Editors' Suggestion

Spin noise spectroscopy of an alignment-based atomic magnetometer

M. Koźbiał,[1,*] L. Elson,[2,*] L. M. Rushton,[2] A. Akbar,[2] A. Meraki,[2] K. Jensen,[2,†] and J. Kołodyński[1,‡]
[1]*Centre for Quantum Optical Technologies, Centre of New Technologies, University of Warsaw, Banacha 2c, 02-097 Warszawa, Poland*
[2]*School of Physics and Astronomy, University of Nottingham, University Park, Nottingham, NG7 2RD, United Kingdom*

(Received 2 January 2024; accepted 7 June 2024; published 30 July 2024)

Optically pumped magnetometers (OPMs) are revolutionizing the task of magnetic-field sensing due to their extremely high sensitivity combined with technological improvements in miniaturization which have led to compact and portable devices. OPMs can be based on spin-oriented or spin-aligned atomic ensembles which are spin polarized through optical pumping with circular or linear polarized light, respectively. Characterization of OPMs and the dynamical properties of their noise is important for applications in real-time sensing tasks. In our work, we experimentally perform spin noise spectroscopy of an alignment-based magnetometer. Moreover, we propose a stochastic model that predicts the noise power spectra exhibited by the device when, apart from the strong magnetic field responsible for the Larmor precession of the spin, white noise is applied in the perpendicular direction aligned with the pumping-probing beam. By varying the strength of the noise applied as well as the linear-polarization angle of incoming light, we verify the model to accurately predict the heights of the Larmor-induced spectral peaks and their corresponding linewidths. Our work paves the way for alignment-based magnetometers to become operational in real-time sensing tasks.

DOI: 10.1103/PhysRevA.110.013125

I. INTRODUCTION

Optically pumped magnetometers (OPMs) [1,2] based on, e.g., caesium, rubidium, or potassium atomic vapor, or helium gas, can have high sensitivity in the fT/$\sqrt{\text{Hz}}$ range [3]. Commercially available OPMs include scalar OPMs for use in, e.g., geophysical surveys [4,5] and zero-field OPMs [5–8] which are promising for applications within areas such as cardiology [9–11] and neuroscience [12–14]. OPMs can also be used for detection of radio-frequency (RF) magnetic fields with potential applications within biomedical imaging [15,16], non-destructive testing [17,18], and remote sensing [19,20]. However, such RF OPMs are not yet commercially available. Orientation-based RF OPMs are typically implemented using two or three laser beams [21–23]. On the other hand, alignment-based RF OPMs implemented with a single laser beam [24] are promising for applications and commercialization [25].

In an optical magnetometer, the atoms are spin polarized using light through the process of optical pumping [26]. In an orientation-based optical magnetometer, the atoms are optically pumped with circularly polarized light. In this case, each atom can be effectively treated as a spin-$\frac{1}{2}$ particle, even if the ground state of the atom has a total angular momentum F larger than $\frac{1}{2}$. The evolution of the atomic spin in a magnetic field is then well described by the Bloch equation for the spin vector $\boldsymbol{F} = (F_x, F_y, F_z)^{\mathrm{T}}$. Its three components correspond to the expectation values of the angular momentum operators defined along the respective directions, i.e., $F_\alpha := \mathrm{Tr}\{\hat{F}_\alpha \rho\}$ with $\alpha = x, y, z$ for an atomic ensemble being effectively described by a single-atom density matrix ρ. On the contrary, in an alignment-based magnetometer [24,25,27–30] the atoms are optically pumped with linearly polarized light. In this case, each atom can be effectively treated as a spin-1 particle [31]. As a result, one has to abandon describing the atomic state with a three-component vector, and instead describe it using rank-2 spherical tensors with five components, which describe how the atomic spin is aligned along certain axes [32].

The purpose of *spin noise spectroscopy* (SNS) [33] is to characterize the noise properties of a given atomic system and, in particular, the form of the autocorrelation function that noise fluctuations exhibit in the steady-state regime [34]. However, only in the case of orientation-based magnetometers have stochastic noise models been proposed that are capable of explaining the observed noise power spectra when probing unpolarized atomic ensembles [35–38], also including the effects of spin-exchange collisions [39–41]. In contrast, such models characterizing fully the spin noise spectra in alignment-based magnetometers are still missing, despite recent promising steps in that direction [42–47].

In our work, we employ methods of stochastic calculus and the formalism of spherical tensors to predict the *power spectral density* (PSD) of an alignment-based magnetometer in the presence of a strong static magnetic field affected by white noise that is applied in the perpendicular direction, i.e., along the beam simultaneously pumping and probing the

*These authors contributed equally to this work.
†Contact author: kasjensendk@gmail.com
‡Contact author: jan.kolodynski@cent.uw.edu.pl

Published by the American Physical Society under the terms of the Creative Commons Attribution 4.0 International license. Further distribution of this work must maintain attribution to the author(s) and the published article's title, journal citation, and DOI.

ensemble. [1] Our model correctly predicts the existence of peaks in the measured PSD at particular multiples of the Larmor frequency, as well as the dependence of their amplitudes and widths on the system geometry and the noise intensity. Importantly, we verify our model in a series of experiments, whose results show very good accordance with the predictions.

Our work paves the way for exploring alignment-based magnetometers in real-time sensing tasks, in which, thanks to the detailed characterization of the spin noise, one is capable of tracking time-varying signals beyond the nominal bandwidth dictated by the magnetometer [48]. Our alignment-based magnetometer with added noise can be used as a scalar magnetometer to sense time-varying magnetic fields, but also potentially ones that oscillate at RF. Thanks to employing only a single beam of light for both pumping and probing the atoms, the simplicity of the proposed architecture is promising with respect to potential miniaturization and commercialization [49].

The remainder of the paper is organized as follows. We first describe the spatial configuration of the magnetometer considered in Sec. II, in order to motivate and explain the spherical-tensor formalism that we particularly employ to parametrize its atomic state in Sec. II A. In Sec. II B we then discuss the evolution of the atomic state and, in particular, how it determines the dynamics of relevant spherical-tensor components and the detected signal, so that in Sec. II C we may relate it to and describe in detail the physical parameters of our experimental setup. In Sec. III we turn to SNS that constitutes the goal of our work. We first explain in Sec. III A what the form of PSD is that we expect for the magnetometer considered, and how we predict it. The results of the experiment are then shown in Sec. III B and compared to the theory in Secs. III B 1 and III B 2. Finally, we conclude in Sec. IV.

II. ALIGNMENT-BASED ATOMIC MAGNETOMETER

In Fig. 1 we depict the natural spatial configuration of an alignment-based atomic magnetometer [24], which applies to the implementation considered here. A strong magnetic field $\boldsymbol{B}_0$, directed along z, acts perpendicularly to the direction of light propagation, here chosen to be x, with light being linearly polarized at an angle θ to z axis in the yz plane. Both the field and the light interact with an atom and modify its steady state, otherwise induced solely by the relaxation processes [27]. Although we defer the formal description of the atomic steady state, let us note for now that its form can be conveniently represented by the *angular-momentum probability surface* [32,50] (depicted in blue in Fig. 1). As the surface describes the effective polarization of the steady state, it indicates the rotational symmetries the state possesses. Its shape strongly depends on the polarization angle θ of the input light beam, e.g., resembling a "peanut" for $\theta = 0$ or a "doughnut" for $\theta = \frac{\pi}{2}$ [see Figs. 1(a) and 1(b), respectively]. As such a qualitative description, however, relies solely on symmetry arguments, it applies irrespectively of other properties of the input light, e.g., its detuning.

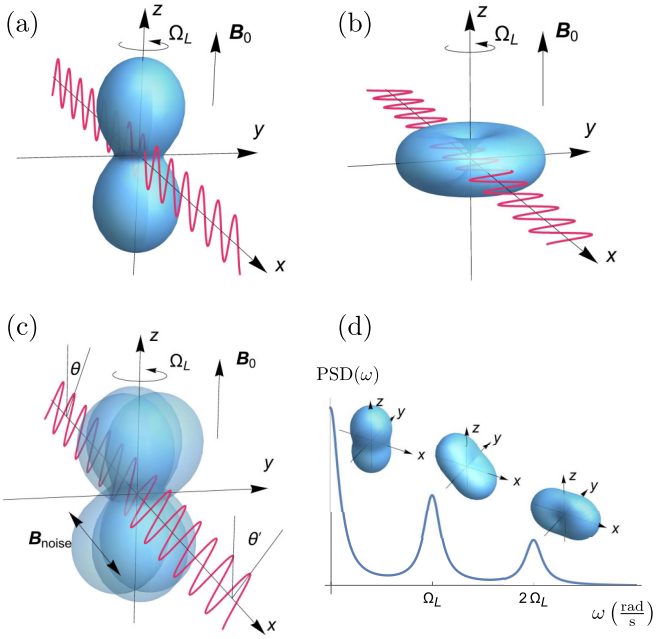

FIG. 1. Alignment-based magnetometer: spatial configuration. The light propagates in the direction x in the presence of a strong, static magnetic field $\boldsymbol{B}_0$, pointing along the z direction. In (a) and (b), angular-momentum probability surfaces of the resulting atomic steady state are presented, when the atom is pumped by vertically ($\theta = 0$) or horizontally ($\theta = \pi/2$) polarized light, respectively. As shown in (c), considering the input light beam to be polarized at some intermediate angle $0 < \theta < \pi/2$, the atomic steady state generally modifies the polarization angle of the transmitted light θ'. Moreover, in our experiment a stochastic field $\boldsymbol{B}_{\text{noise}}$ is applied along the direction of light propagation, and induces white noise that disturbs the atomic state from equilibrium. The so-created randomly tilted state has now three distinct contributions from spherical components $\mathcal{T}^{(2)}_0$, $\mathcal{T}^{(2)}_{\pm 1}$, and $\mathcal{T}^{(2)}_{\pm 2}$, whose angular-momentum probability surfaces shown in (d) exhibit periodicity under rotations around z at multiples 0, Ω_L, and $2\Omega_L$ of the Larmor (angular) frequency Ω_L, respectively. As a result, as depicted in (d), the recorded *power spectral density* (PSD) of θ' fluctuations should contain three peaks at these particular frequencies with amplitudes dictated by the contribution of each spherical-tensor component.

Importantly, in our experiment the atom is further disturbed by a stochastic field $\boldsymbol{B}_{\text{noise}}$ [see Fig. 1(c)], that induces white noise along the x direction, whose impact can then be monitored by inspecting the polarization angle θ' of the transmitted beam, while the atomic state is constantly "kicked out" of equilibrium. As we carry out the experiment in conditions in which correlations between distinct atoms may be neglected during the sensing process, the dynamics of the whole ensemble is effectively captured by the evolution of a single atom [26]. Furthermore, due to the effective atomic density being low, the shot noise of the photon-detection process dominates over the atomic projection noise, and the impact of the measurement back-action on the atomic steady state can be ignored [51,52]. Moreover, thanks to the presence of

[1] In contrast to the parallel configuration, in which the white noise would just yield effective fluctuations of the static field [47].

a relatively strong magnetic field $\boldsymbol{B}_0$, given that the experiment is carried out at room temperature, the mechanism of spin-exchange interactions during atomic collisions is irrelevant [53], in contrast to SERF magnetometers [54], that could in principle induce not only classical correlations but also entanglement between individual atoms [55,56].

In what follows, we first formalize the description of an atomic steady state in the spherical-tensor representation, in order to then show how such a formalism allows us to compactly model the magnetometer dynamics, as well as predict the behavior of the detected signal.

A. Spherical-tensor representation of the atomic steady state

Any density matrix describing an atom of total angular momentum F can always be written in the eigenbasis of the angular-momentum operators $\hat{F}^2$ and $\hat{F}_z$ as [26]

$$\rho^{(F)} = \sum_{M,M'=-F}^{F} \rho^{(F)}_{MM'} |F, M\rangle\langle F, M'|. \tag{1}$$

However, it is much more convenient to decompose the density matrix in the basis of *spherical-tensor operators* of rank $\kappa = 0, 1, \ldots, 2F$, which transform independently in each κ subspace under rotations, and hence magnetic fields, in a well-behaved manner. In particular, the atomic state of fixed F in Eq. (1) can be generally written as

$$\rho^{(F)} = \sum_{\kappa=0}^{2F} \sum_{q=-\kappa}^{\kappa} m^{(F)}_{\kappa q}\, \mathcal{T}^{(\kappa)}_q(F), \tag{2}$$

where the density matrix is now decomposed into a sum of rank-κ *components*, each constituting a sum (over q) of, in principle, non-Hermitian *tensor operators* $\mathcal{T}^{(\kappa)}_q(F)$ (see, e.g., [26] and Appendix A) multiplied by their corresponding complex *coefficients* $m^{(F)}_{\kappa q}$. For a given fixed F, $\mathcal{T}^{(\kappa)}_q$ form a basis and they formally satisfy $\mathrm{Tr}\{\mathcal{T}^{(\kappa)}_q(\mathcal{T}^{(\kappa')}_{q'})^\dagger\} = \delta_{\kappa\kappa'}\delta_{qq'}$, while it is convenient to also impose $\mathcal{T}^{(\kappa)\dagger}_q = (-1)^q\mathcal{T}^{(\kappa)}_{-q}$, so that conditions $m_{\kappa q} = (-1)^q m^*_{\kappa,-q}$ and $\mathrm{Im}\{m_{\kappa 0}\} = 0$ ensure then the density matrix (2) is Hermitian. The $m_{00} = 1/\sqrt{2F+1}$ coefficient is fixed by the $\mathrm{Tr}\rho = 1$ condition, while the corresponding ($\kappa = 0$) tensor operator $\mathcal{T}^{(0)}_0 = \frac{1}{\sqrt{2F+1}}\mathbb{1}_{2F+1}$ is the only one with a nonzero trace, being invariant under any rotations.

In principle, the atomic steady state may involve more than one F level, e.g., $F = 3, 4$ in the case of the D1-line transition in caesium. However, if the laser field is tuned to a specific optical transition from a single F level, and there is no coherent coupling between levels of different F, one can disregard coherences between these and most generally write the atomic steady state as

$$\rho = \bigoplus_F p_F\, \rho^{(F)}, \tag{3}$$

where p_F is the effective fraction of atoms having the total angular momentum F. Moreover, one may then focus on the dynamics of only one particular $\rho^{(F)}$ for the F level actually contributing to the light-atom interaction, with $\rho^{(F)}$ being then decomposable just as in Eq. (2). In such a case, as done in what follows, the (F) superscript can be dropped for simplicity.

As the case of a *linearly polarized* pump is of our interest (see Fig. 1), from symmetry arguments it follows that, independently of the spin number F, only even-κ coefficients are modified when interacting with light [57]. Moreover, as we show later, our model predicts no significant coupling between components of different κ. On the other hand, it is only the *orientation* ($\kappa = 1$) and *alignment* ($\kappa = 2$) components that can be probed by resorting to electric dipole light-atom interactions [26,57]. Hence, even though the pump in the experiment is relatively strong, so that the atomic state in Eq. (2) reads as

$$\rho = \frac{1}{2F+1}\mathbb{1}_{2F+1} + \sum_{q=-2}^{2} m_{2q}\mathcal{T}^{(2)}_q + \sum_{q=-4}^{4} m_{4q}\mathcal{T}^{(4)}_q + \cdots, \tag{4}$$

any detection signal obtained by probing the atoms with light is determined by the vector containing the alignment coefficients:

$$\mathbf{m} = (m_{2,-2} \quad m_{2,-1} \quad m_{2,0} \quad m_{2,1} \quad m_{2,2})^{\mathrm{T}}, \tag{5}$$

whose dynamics must therefore only be tracked.

Furthermore, if the quantization axis z is chosen along the light polarization of the pump, $\theta = 0$ in Fig. 1(a), by symmetry the atomic steady state must be invariant to any rotations around z. Hence, only the (real) coefficient with $q = 0$ can acquire some value $m_{2,0} \to m^{\mathrm{ini}}_{20}$, whose maximum (or negative minimum) is theoretically constrained by the positivity of $\rho \geqslant 0$, but practically by the efficiency of optical pumping being counteracted by relaxation. Considering the light to be linearly polarized at an arbitrary angle to the xz plane [see Fig. 1(c)], the steady state can be found by just adequately rotating the above solution for $\theta = 0$ around the light-propagation direction x. In particular, the $\mathbf{m}$ vector (5) of the *steady state* (ss) generated by linearly polarized pump at an angle θ with respect to the quantization axis reads as (see Appendix A)

$$\mathbf{m}^{\mathrm{ss}} = m^{\mathrm{ini}}_{20}\Big(-\tfrac{\sqrt{6}}{4}\mathtt{s}^2_\theta \quad i\tfrac{\sqrt{6}}{4}\mathtt{s}_{2\theta} \quad 1-\tfrac{3}{2}\mathtt{s}^2_\theta \quad i\tfrac{\sqrt{6}}{4}\mathtt{s}_{2\theta} \quad -\tfrac{\sqrt{6}}{4}\mathtt{s}^2_\theta\Big)^{\mathrm{T}}, \tag{6}$$

where $\mathtt{s}_\theta := \sin\theta$. However, as the strong static field $\boldsymbol{B}_0$ leads to (Larmor) precession of the atomic state around z (see Fig. 1) that is much faster than the timescale of reaching the steady state, i.e., with the Larmor (angular) frequency $\Omega_L := \gamma_{\mathrm{gmr}}|\boldsymbol{B}_0|$ much greater than the overall relaxation rate, all the multipoles $m_{2,q\neq 0}$ quickly average to zero, so that according to the secular approximation [26] the steady-state vector (6) simplifies to

$$\mathbf{m}^{\mathrm{ss}} \approx m^{\mathrm{ini}}_{20}\big(0 \quad 0 \quad 1-\tfrac{3}{2}\sin^2\theta \quad 0 \quad 0\big)^{\mathrm{T}}, \tag{7}$$

which we assume to be valid throughout this work. The Larmor frequency above is defined using the gyromagnetic ratio $\gamma_{\mathrm{gmr}} := g_F\mu_B/\hbar$ (with units $[\mathrm{rad\,s^{-1}T^{-1}}]$), where g_F is the Landé g factor for an atom of total spin F and μ_B is the Bohr magneton.

In order to visualize the symmetries and geometric properties of the steady state (7), we resort to plotting the

angular-momentum probability surfaces it yields for $\theta = 0$, $\theta = \frac{\pi}{2}$, and $0 < \theta < \frac{\pi}{2}$ in Figs. 1(a)–1(c), respectively. In particular, in each case we present a spherical plot of the overlap of the steady state with the state of a maximum angular momentum $|F, F\rangle_{\boldsymbol{n}}$ defined with respect to a given direction $\boldsymbol{n}$, which then determines the quantization axis, i.e.,

$$r(\boldsymbol{n}) = {}_{\boldsymbol{n}}\langle F, F|\rho_{\rm ss}|F, F\rangle_{\boldsymbol{n}}, \tag{8}$$

where $\rho_{\rm ss}$ is the steady-state density matrix of the form (4) with the alignment coefficients given by Eq. (7).

In our experiment, as shown in Fig. 1(c), the angular-momentum probability surface of the steady state is constantly perturbed out of equilibrium by the $\boldsymbol{B}_{\rm noise}$ field inducing white noise in the x direction, so that coefficients with $q \neq 0$ in Eq. (7) are no longer zero. As a result, the effective atomic state contains components not only from $\mathcal{T}^{(2)}_0$, but also from $\mathcal{T}^{(2)}_{\pm 1}$ and $\mathcal{T}^{(2)}_{\pm 2}$ tensor operators [see Eq. (4)], which can be separately visualized by the surfaces depicted in Fig. 1(d). Crucially, as the latter two return to their original state under Larmor precession after being rotated by 2π and π, respectively, the measured noisy θ' signal should contain distinct frequency components at Ω_L and $2\Omega_L$. This should be visible when analyzing the *power spectral density* (PSD) of the detected signal, as schematically presented in Fig. 1(d).

B. Magnetometer dynamics and measurement

In order to be able to predict the PSD in our experiment, we must move away from just the steady-state description. In particular, we must be able to model the stochastic dynamics of the atoms, so that the autocorrelation function of the detected signal can be computed, whose Fourier transform specifies the PSD.

1. Atomic stochastic dynamics

Dissipative nonunitary evolution. A dissipative evolution of the atomic state (1) is generally described by the Gorini-Kossakowski-Sudarshan-Lindblad equation [58]

$$\frac{d\rho}{dt} = -\frac{i}{\hbar}[\hat{H}, \rho] + \Phi[\rho], \tag{9}$$

where $\hat{H}$ is the system Hamiltonian, while the map

$$\Phi[\rho] = \sum_i \Gamma_i \left(\hat{L}_i \rho \hat{L}_i^\dagger - \frac{1}{2}\{\hat{L}_i^\dagger \hat{L}_i, \rho\} \right) \tag{10}$$

is responsible for the decoherence, with $\hat{L}_i$ being the quantum jump (Lindblad) operators and $\Gamma_i \geqslant 0$ the corresponding dissipation rates, which must be non-negative for a Markovian evolution [58].

In the absence of the $\boldsymbol{B}_{\rm noise}$ field, the Hamiltonian incorporates only the interaction of the atom with the static field, i.e., $\hat{H} = \gamma_{\rm gmr}\boldsymbol{B}_0 \cdot \hat{\boldsymbol{F}} = \Omega_L \hat{F}_z$. However, as the static field introduces anisotropicity in the system, we split the decoherence map as follows:

$$\Phi[\rho] \coloneqq \sum_{\alpha=x,y,z} \Phi_\alpha[\rho] + \Phi_{\rm iso}[\rho], \tag{11}$$

where

$$\Phi_\alpha[\rho] \coloneqq \frac{\Gamma_\alpha}{\hbar^2}\left(\hat{F}_\alpha \rho \hat{F}_\alpha - \frac{1}{2}\{\hat{F}_\alpha^2, \rho\} \right) \tag{12}$$

can be interpreted as arising from magnetic-field fluctuation in each $\alpha = x, y, z$ direction, whereas

$$\Phi_{\rm iso}[\rho] \coloneqq \Gamma_{\rm iso}\left(\sum_{M,M'} \hat{L}_{M,M'} \rho \hat{L}^\dagger_{M,M'} - \frac{1}{2}\{\hat{L}^\dagger_{M,M'}\hat{L}_{M,M'}, \rho\} \right), \tag{13}$$

with $\hat{L}_{M,M'} \coloneqq \frac{1}{\sqrt{2F+1}}|F, M\rangle\langle F, M'|$, represents isotropic dissipation that can be equivalently written as

$$\Phi_{\rm iso}[\rho] = \Lambda - \tfrac{1}{2}\{\hat{\Gamma}, \rho\}, \tag{14}$$

where $\hat{\Gamma} \coloneqq \Gamma_{\rm iso}\mathbb{1}_{2F+1}$ and $\Lambda \coloneqq \frac{\Gamma_{\rm iso}}{2F+1}\mathbb{1}_{2F+1}$ are typically referred to as the repopulation and depolarizing terms, respectively [32]. Although we assume in our model the rates Γ_α and $\Gamma_{\rm iso}$ to be phenomenological and account for various dissipation mechanisms, Eq. (14) can be naturally interpreted as the loss of polarized atoms that then reappear in the beam in a completely unpolarized state.

Impact of the stochastic $\boldsymbol{B}_{\rm noise}$ *field.* In our experiment [see Fig. 1(c)], stochastic $\boldsymbol{B}_{\rm noise}$ field is applied in the light-propagation direction x, which leads to another term in the Hamiltonian $\hat{H}_{\rm noise}(t) = \gamma_{\rm gmr}\boldsymbol{B}_{\rm noise}(t) \cdot \hat{\boldsymbol{F}} = \gamma_{\rm gmr}B_{\rm noise}(t)\hat{F}_x$ with

$$B_{\rm noise}(t) = \frac{\Omega_{\rm noise}}{\gamma_{\rm gmr}}\xi(t) \approx \frac{\Omega_{\rm noise}}{\gamma_{\rm gmr}}\sqrt{\frac{1}{2\pi\,\Delta f}}\frac{dW_t}{dt}, \tag{15}$$

where $\Omega_{\rm noise}$ is an effective magnetic noise amplitude given in the units of Larmor frequency, while $\xi(t)$ represents the stochastic process for the noise we generate (see Appendix C for its further characteristics), which effectively exhibits a constant power spectrum in a frequency range $f \in [\delta f, f_{\rm cutoff}]$ (in Hz) with δf set close to zero to eliminate spurious low-frequency contributions, and some large cutoff $f_{\rm cutoff}$ imposed to prevent the effect of aliasing. Now, as we will deal with processes occurring at (angular) frequencies $\omega \approx \Omega_L$, such noise in Eq. (15) can be effectively described as white with the correct rescaling factor $\Delta f \coloneqq f_{\rm cutoff} - \delta f \approx f_{\rm cutoff}$; the white noise can be interpreted as the time derivative $\frac{dW}{dt}$ of the Wiener process W_t [59]. As a result, we can write the (stochastic) time increment induced by the noise involving the Hamiltonian as

$$\hat{H}_{\rm noise}(t)dt = \sqrt{\omega_{\rm noise}}\,\hat{F}_x\,dW_t, \tag{16}$$

where we define $\omega_{\rm noise} \coloneqq \Omega^2_{\rm noise}/(2\pi f_{\rm cutoff})$ as the effective *noise spectral density*, while $dW_t \sim \mathcal{N}(0, dt)$ is then normally distributed with variance dt, i.e., the Wiener increment [59].

In order to correctly include the white noise in the deterministic dynamics (9), we must explicitly compute the time increment of the density matrix $d\rho = \rho(t + dt) - \rho(t)$, that is now stochastic. By adding the noise contribution to Eq. (9), we define the stochastic map

$$\mathcal{K}(t)[\rho] \coloneqq -\frac{i}{\hbar}[\hat{H}_{\rm noise}(t) + \hat{H}, \rho] + \Phi[\rho], \tag{17}$$

which allows us to write for small dt

$$\begin{aligned}\rho(t+dt) &= e^{\mathcal{K}(t)dt}[\rho(t)] = \sum_{n=0}^{\infty}\frac{[\mathcal{K}(t)dt]^n[\rho(t)]}{n!}\\ &= \rho(t)+\mathcal{K}[\rho(t)]dt+\frac{1}{2}(\mathcal{K}dt)^2[\rho(t)]+O(dt^{5/2})\\ &= \rho(t)-\frac{i}{\hbar}[\hat{H},\rho(t)]dt+\Phi[\rho(t)]dt\\ &\quad -\frac{i\sqrt{\omega_{\text{noise}}}}{\hbar}[\hat{F}_x,\rho(t)]dW_t-\frac{\omega_{\text{noise}}}{2\hbar^2}[\hat{F}_x,[\hat{F}_x,\rho(t)]]dt\\ &\quad +O(dt^{3/2}),\end{aligned} \tag{18}$$

where according to the Itô calculus implying $dW_t^2 = dt$ we obtain a dissipative term at the second ($n = 2$) order, while all the other terms can be ignored with $dW_t dt = O(dt^{3/2})$ within the big-O notation [59].

As a consequence, we obtain the desired stochastic differential equation describing the atomic dynamics as

$$\begin{aligned}d\rho &= \left(-\frac{i}{\hbar}[\hat{H},\rho]+\Phi_{\text{iso}}[\rho]\right)dt\\ &\quad +\sum_{\alpha=y,z}\frac{\Gamma_\alpha}{\hbar^2}\left(\hat{F}_\alpha\rho\hat{F}_\alpha-\frac{1}{2}\{\hat{F}_\alpha^2,\rho\}\right)dt\\ &\quad +\frac{\Gamma_x+\omega_{\text{noise}}}{\hbar^2}\left(\hat{F}_x\rho\hat{F}_x-\frac{1}{2}\{\hat{F}_x^2,\rho\}\right)dt\\ &\quad -\frac{i\sqrt{\omega_{\text{noise}}}}{\hbar}[\hat{F}_x,\rho]dW_t,\end{aligned} \tag{19}$$

which, apart from the expected term generating random rotations around the $\boldsymbol{B}_{\text{noise}}$-field direction, accounts for the fact that (by the fluctuation-dissipation theorem) the white noise must also increase the dissipation rate in the x direction from Γ_x to $\Gamma_x+\omega_{\text{noise}}$.

2. Spherical-tensor representation

We have argued that when considering the relevant F subspace of the atomic steady state described in Eq. (2), the nature and geometry of light-atom interactions allows us to reduce its form, so that it contains only the alignment component ($\kappa = 2$) in Eq. (4). Consistently, as shown in Appendix A, the evolution determined by Eq. (19) does not couple spherical-tensor components of different rank κ. Hence, while incorporating optical pumping into the dynamics (19), the evolution of the atomic state must be completely described by the $\mathbf{m}$ vector (5) of, now time-dependent, alignment coefficients, i.e.,

$$\mathbf{m}_t = (m_{2,-2}(t)\quad m_{2,-1}(t)\quad m_{2,0}(t)\quad m_{2,1}(t)\quad m_{2,2}(t))^{\mathrm{T}}. \tag{20}$$

This evolves under the dynamics (19) according to the following stochastic differential equation (see Appendix A):

$$d\mathbf{m}_t = \left(\mathbf{A}_0+\mathbf{A}_\Phi+\frac{\mathbf{A}_{\text{noise}}^2}{2}\right)\mathbf{m}_t\,dt+\mathbf{A}_{\text{noise}}\,\mathbf{m}_t\,dW_t, \tag{21}$$

where $\mathbf{A}_0 = -i\Omega_L\mathbf{J}_z^{(2)}$ and $\mathbf{A}_{\text{noise}} = -i\sqrt{\omega_{\text{noise}}}\mathbf{J}_x^{(2)}$ are 5×5 matrices that should be associated with the free evolution and stochastic noise, respectively. These are defined with help of the representation of angular momentum operators $\mathbf{J}_\alpha^{(\kappa)}$, with $\alpha = x, y, z$, acting on the vector space of alignment, equivalent to ones acting on the state space of a spin-2 particle, written in the $\{|2,-2\rangle,\ldots,|2,2\rangle\}$ basis to agree with Eq. (20).

In a similar fashion, the matrix representation of the dissipative map Φ in Eq. (11) (see Appendix A) reads as

$$\begin{aligned}\mathbf{A}_\Phi &= -\frac{1}{2}\sum_\alpha\Gamma_\alpha\left(\mathbf{J}_\alpha^{(2)}\right)^2-\Gamma_{\text{iso}}\mathbb{1}_5\\ &\equiv -\text{diag}\{\Gamma_2,\Gamma_1,\Gamma_0,\Gamma_1,\Gamma_2\},\end{aligned} \tag{22}$$

which we, however, force above to have a diagonal form postulated in Ref. [27] with three dissipation rates:

$$\boldsymbol{\Gamma}\equiv\begin{pmatrix}\Gamma_0\\ \Gamma_1\\ \Gamma_2\end{pmatrix}\coloneqq\begin{pmatrix}6\Gamma_\perp+\Gamma_{\text{iso}}\\ \Gamma_\parallel+5\Gamma_\perp+\Gamma_{\text{iso}}\\ 4\Gamma_\parallel+2\Gamma_\perp+\Gamma_{\text{iso}}\end{pmatrix}. \tag{23}$$

Formally, this corresponds to the assumption that in the absence of the induced magnetic-field noise one should differentiate only between dephasing rates along, $\Gamma_\parallel\coloneqq\Gamma_z$, and perpendicular to, $\Gamma_\perp\coloneqq\Gamma_x=\Gamma_y$, the static field, while keeping the isotropic depolarization rate Γ_{iso} as an independent parameter. The effective rates $\boldsymbol{\Gamma}$ (see also Appendix A) are then defined by reparametrizing the problem as in Eq. (23).

Finally, in order to include the impact of optical pumping in Eq. (21), we enforce that, in the absence of the noisy magnetic field, the $\mathbf{m}_t$ vector (20) must converge with time to the steady state described in Sec. II A. This way, we obtain the desired stochastic dynamical equation for the vector of alignment coefficients as

$$\begin{aligned}d\mathbf{m}_t &= \left(\mathbf{A}_0+\frac{\mathbf{A}_{\text{noise}}^2}{2}\right)\mathbf{m}_t\,dt+\mathbf{A}_\Phi(\mathbf{m}_t-\mathbf{m}^{\text{ss}})\,dt\\ &\quad +\mathbf{A}_{\text{noise}}\mathbf{m}_t\,dW_t,\end{aligned} \tag{24}$$

where the steady state $\mathbf{m}^{\text{ss}}$ is given by Eq. (7), being already averaged over the fast (Larmor) precession around z and, hence, satisfying $\mathbf{A}_0\mathbf{m}^{\text{ss}} = \mathbf{0}$.

3. Detected signal

We depict the phenomenon of polarization rotation in Fig. 1(c), i.e., the effect that the angle θ of the linearly polarized incoming beam is changed to θ' upon leaving the atomic cell. Treating the atomic ensemble as an optically thin sample, the change of the angle $\Delta\theta\coloneqq\theta'-\theta$ obeys then [32,60]

$$\Delta\theta\propto i(\tilde{m}_{2,1}+\tilde{m}_{2,-1}), \tag{25}$$

with the proportionality constant depending on the optical depth, interaction strength, light power, etc.

In the above, $\tilde{m}_{\kappa,q}$ are the alignment coefficients defined with the quantization axis along the direction of incoming light polarization, i.e., tilted away by θ from z in the yz plane [see Fig. 1(c)]. Hence, Eq. (25) can be reexpressed with help of the $\mathbf{m}_t$ vector (20) (defined with z being the quantization axis) by simply rotating $\mathbf{m}_t$ by an angle θ around the light-propagation direction x, i.e.,

$$\Delta\theta\propto\mathbf{h}^{\mathrm{T}}\,\mathbf{D}_\theta^{(2)}\mathbf{m}_t, \tag{26}$$

where $\mathbf{h} = (0,i,0,i,0)^{\mathrm{T}}$ and $\mathbf{D}_\theta^{(2)} = D_{m,m'}^{(2)}(-\pi/2,\theta,\pi/2)$ is the appropriate Wigner D-matrix (see Appendix A).

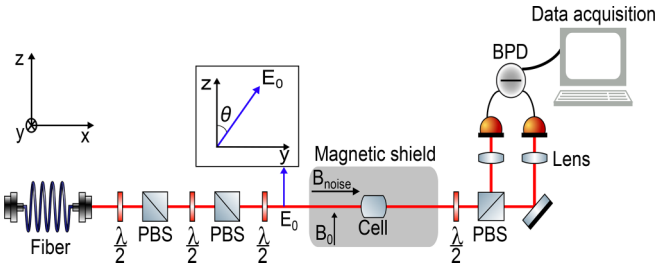

FIG. 2. Alignment-based magnetometer: experimental setup. Linearly polarized light is passed through a polarization maintaining fiber. Two sets of half-wave plates ($\lambda/2$) and polarizing beam splitters (PBS) are used to reduce intensity fluctuations and to change the power of the laser beam, respectively. The laser light propagates along the x direction, while the angle θ of its linear polarization is then adjusted by rotating yet another half-wave plate, before it enters the magnetic shield (marked in gray). Within the shield, the light simultaneously pumps and probes the atomic ensemble of caesium atoms contained within a paraffin-coated cell (cell). The atoms are subject to (strong) static and (relatively weak) noisy magnetic fields: $\boldsymbol{B}_0$ applied in the z direction and $\boldsymbol{B}_{\text{noise}}$ applied in the x direction, respectively. Upon interacting with the atoms, the polarization of light undergoes rotation, which is then measured by passing the output beam through a PBS and performing balanced photodetection (BPD).

As a result, based on Eq. (26), we may write the detected signal of an alignment-based magnetometer as

$$\begin{aligned} S(t) &= g_D\, \mathbf{h}^{\mathrm{T}}\, \mathbf{D}_{\theta}^{(2)} \mathbf{m}_t + \zeta(t) \\ &= g_D\, \tfrac{1}{2}[\sqrt{6} m_{2,0}(t) + m_{2,2}(t) + m_{2,-2}(t)] \sin(2\theta) \\ &\quad + g_D\, i[m_{2,1}(t) + m_{2,-1}(t)] \cos(2\theta) + \zeta(t), \end{aligned} \tag{27}$$

where g_D is the effective proportionality constant, whereas $\zeta(t)$ denotes the detection noise, which is completely uncorrelated from the magnetic-field noise affecting the atom dynamics in Eq. (24). Moreover, as we assume here the impact of the measurement back-action exerted on the atomic state by the light to be ignorable [51,52], $\zeta(t)$ shall not exhibit any correlations with any noise exhibited by the atoms.

It becomes clear from the expression (27) that, as the signal depends on all the alignment coefficients with $q = 0, \pm 1, \pm 2$, it must contain components that oscillate at frequencies 0, Ω_L, and $2\Omega_L$, respectively. In other words, the signal contains information about different spherical-tensor components of the atomic state, in particular the ones illustrated in Fig. 1(d), each of which should yield a peak in the PSD at the corresponding frequency.

C. Experimental setup

Figure 2 shows a schematic of the experimental setup we employ. Linearly polarized light, with a wavelength of 895 nm, is passed through a polarization-maintaining optical fiber. The light is resonant with the $F = 4 \rightarrow F' = 3$ D1 transition of caesium. The light has an electric field vector $\boldsymbol{E}_0$ and passes through a cubic paraffin-coated cell containing caesium atoms, which is placed inside a magnetic shield (Twinleaf MS-1). The cell is $(5\ \text{mm})^3$ and is kept at room temperature ($\sim 18^\circ$). The laser beam diameter is ~ 2 mm.

A static magnetic field $\boldsymbol{B}_0 = B_0\, \boldsymbol{e}_z$ is applied using the magnetic shield coils. A half-wave plate is placed before the magnetic shield to change the angle of the electric-field vector of the light $\boldsymbol{E}_0$, with respect to the direction of the static magnetic field. Consistently with Fig. 1(c), we denote in Fig. 2 by θ the angle between the linear polarization and the z direction in the yz plane, so that, e.g., $\boldsymbol{E}_0 = E_0\, \boldsymbol{e}_z$ for $\theta = 0$ and $\boldsymbol{E}_0 = E_0\, \boldsymbol{e}_y$ for $\theta = \pi/2$. In parallel, a noisy magnetic field $\boldsymbol{B}_{\text{noise}}(t) = B_{\text{noise}}(t)\, \boldsymbol{e}_x$ is applied to the system using a homemade square Helmholtz coil. The current driving the coil corresponds to the white-noise signal outputted by a function generator, which is, however, first transformed thorough a $f_{\text{cutoff}} = 1$ MHz low-pass filter to prevent the effect of aliasing, as well as a $\delta f = 1$ kHz high-pass filter to eliminate any spurious contributions at very low frequencies (see Appendix D for more details).

When measuring the power spectra of our magnetometer as a function of the strength of the noisy magnetic field, as described below, we set the static magnetic field to $B_0 = 2.7\ \mu$T, what corresponds to inducing the Larmor precession of the atomic spin at a frequency $f_L \approx 9.45$ kHz. In such a case, each data set is acquired for a given fixed white-noise amplitude in the range of 70.91 nT_{rms}, for the first set, to 35.45 μT_{rms}, for the final data set. When investigating the dependence on the polarization angle θ instead, we use the static field $B_0 = 2.74\ \mu$T (i.e., $f_L \approx 9.6$ kHz), while the white-noise amplitude is fixed to 1.4 μT_{rms}.

As shown in Fig. 2, after the magnetic shield the polarization rotation of the transmitted light is measured using a half-wave plate ($\lambda/2$) and a polarizing beam splitter (PBS). The linear polarization of the setup was checked before and after the vapor cell, by measuring the ellipticity of the beam which was found to be of negligible order. The half-wave plate is rotated to match exactly the polarization angle θ' of the transmitted light [see Fig. 1(c)], so that it is the deviations from θ' that are then effectively measured via balanced photodection (BPD).[2] In particular, the difference in the intensity of the outgoing beams from the PBS is tracked using a Thorlabs balanced photodetector (PDB210A/M). The output photocurrent is recorded in real time using a data acquisition card. Further technical details about the performance of the magnetometer used can be found in Ref. [25].

Importantly, as our experiment matches the spatial configuration of an alignment-based magnetometer described in previous sections, we can interpret the measured photocurrent of the BPD exactly as

$$\delta S(t) := S(t) - \bar{S}, \tag{28}$$

where by $\bar{S} := \langle S(t) \rangle_{\text{ss}}$ we denote the time-independent mean DC component of the measured signal, which is determined by the mean of the steady-state solution of Eq. (24). As a result, Eq. (28) describes deviations from the mean value of the detected signal stated in Eq. (27). The effective proportionality constant g_D in Eq. (27), which relates the instantaneous

[2]Even if θ' is not exactly matched, the resulting DC component of the detected signal (27) yields a spike at zero frequency in the PSD, whose presence may be safely ignored within our analysis.

atomic state to the photocurrent signal, is then dictated by a number of experimental conditions including the light power ($1\ \mu W$), pumping efficiency, size of the vapor cell [$(5\ \text{mm})^3$], as well as the temperature (room temperature, $\sim 18°\text{C}$). On the other hand, the detection noise, $\zeta(t)$ in Eq. (27), should be attributed to photon shot noise and electronic jitter arising solely due to the photodetection process that effectively leads to a background noise; within the measured PSD a DC offset is observed independently whether the light beam interacts with the atoms or not. This results in a noise floor that depends on the frequency, partially due to the $1/f$ noise. This will be taken into account when interpreting the data in Sec. III B below.

III. SPIN NOISE SPECTROSCOPY

Denoting the Fourier transform of any signal, here the measured current of the balanced photodetector $\delta S(t)$ defined in Eq. (28), over a finite-time interval $[0, T]$ as

$$\delta S(\omega) = \frac{1}{\sqrt{T}} \int_0^T dt\, e^{-i\omega t} \delta S(t), \tag{29}$$

its *power spectral density* (PSD) is defined as [33]

$$\text{PSD}(\omega) \coloneqq \langle |\delta S(\omega)|^2 \rangle, \tag{30}$$

where by $\langle \dots \rangle$ we denote throughout the article an average over stochastic trajectories.

Importantly, provided that $\delta S(t)$ is stationary and ergodic, which can be ensured by letting $T \gg \tau_{\text{coh}}$ in Eq. (29) where τ_{coh} is some effective coherence time of the noisy system under study, we may rewrite the power spectrum according to the Wiener-Khinchin theorem as [33]

$$\text{PSD}(\omega) \underset{\text{ss}}{=} 2 \int_0^\infty dt\, \cos(\omega t) \langle \delta S(t) \delta S(0) \rangle \tag{31a}$$

$$\underset{\text{ss}}{=} 2 \int_0^\infty dt\, \cos(\omega t) \langle S(t), S(0) \rangle, \tag{31b}$$

where by "ss," as before, we emphasize the above to hold in the steady state. In particular [see Eq. (31a)], the PSD (30) can be expressed in terms of the *autocorrelation function* of the (zero-mean) signal $\delta S(t)$ or, equivalently [see Eq. (31b)], the *autocovariance function* of the actual detected signal $S(t)$ specified in Eq. (27), i.e., $\langle S(t_1), S(t_2) \rangle \coloneqq \langle S(t_1) S(t_2) \rangle - \langle S(t_1) \rangle \langle S(t_2) \rangle$ [59].

Substituting explicitly the form of the detected signal (27) into Eq. (31b), we obtain the form of the PSD applicable to our problem as

$$\text{PSD}(\omega) = g_D^2\, \mathbf{h}^{\mathrm{T}}\, \mathbf{D}_\theta^{(2)}\, \boldsymbol{\Xi}(\omega) \mathbf{D}_\theta^{(2)\mathrm{T}} \mathbf{h} + \langle |\zeta(\omega)|^2 \rangle, \tag{32}$$

where the (5×5) matrix $\boldsymbol{\Xi}(\omega)$ is defined as

$$\Xi_{pq}(\omega) \coloneqq 2 \int_0^\infty dt\, \cos(\omega t) \langle m_{2,p}(t), m_{2,q}(0) \rangle, \tag{33}$$

with $p, q = -2, \dots, 2$ specifying the coefficients of the $\mathbf{m}_t$ vector (20) evaluated in the steady state. As the detection noise $\zeta(\omega)$ is uncorrelated from any other noise sources within our model, it leads to a noise floor in Eq. (30) as expected.

A. Theoretical predictions

The alignment dynamics derived in Eq. (24) constitutes an example of a stochastic inhomogeneous evolution [59], for which one can explicitly determine the form of the $\boldsymbol{\Xi}(\omega)$ matrix appearing in the PSD (30) (see Appendix B), i.e.,

$$\boldsymbol{\Xi}(\omega) = (\mathbf{A}_{\text{det}} + i\omega)^{-1} \mathbf{A}_{\text{noise}}\, \boldsymbol{\sigma}\, (\mathbf{A}_{\text{noise}})^{\mathrm{T}} \left(\mathbf{A}_{\text{det}}^{\mathrm{T}} - i\omega\right)^{-1}, \tag{34}$$

where by $\mathbf{A}_{\text{det}} \coloneqq \mathbf{A}_0 + \mathbf{A}_\Phi + \frac{1}{2}\mathbf{A}_{\text{noise}}^2$ we denote for short the overall matrix responsible in Eq. (21) for the deterministic evolution. The (covariance) matrix $\boldsymbol{\sigma}$ above is then (see Appendix B) the solution of the *linear* equation

$$\begin{aligned} &\mathbf{A}_{\text{det}} \boldsymbol{\sigma} + \boldsymbol{\sigma} \mathbf{A}_{\text{det}}^{\mathrm{T}} + \mathbf{A}_{\text{noise}}\, \boldsymbol{\sigma}\, (\mathbf{A}_{\text{noise}})^{\mathrm{T}} \\ &\quad = \mathbf{A}_\Phi \mathbf{m}^{\text{ss}} (\mathbf{m}^{\text{ss}})^{\mathrm{T}} \mathbf{A}_\Phi{}^{\mathrm{T}} \left(\mathbf{A}_{\text{det}}^{\mathrm{T}}\right)^{-1} \\ &\qquad + (\mathbf{A}_{\text{det}})^{-1} \mathbf{A}_\Phi \mathbf{m}^{\text{ss}} (\mathbf{m}^{\text{ss}})^{\mathrm{T}} \mathbf{A}_\Phi{}^{\mathrm{T}}, \end{aligned} \tag{35}$$

which can always be solved fast numerically, given $\mathbf{A}_0$, $\mathbf{A}_{\text{noise}}$, $\mathbf{A}_\Phi$, and $\mathbf{m}^{\text{ss}}$.

However, independently of the particular form of $\boldsymbol{\sigma}$, one can show that the PSD (32) for our problem (see Appendix B) must correspond to a sum of absorptive and dispersive Lorentzian functions:

$$\begin{aligned} \text{PSD}(\omega) = &\sum_{j=-2,\dots,2} \frac{p^a_{|j|} \gamma^2_{|j|}}{(\omega - \omega_j)^2 + \gamma^2_{|j|}} \\ &+ \sum_{j=\pm 1, \pm 2} \frac{\pm p^d_{|j|} \gamma_{|j|} (\omega - \omega_j)}{(\omega - \omega_j)^2 + \gamma^2_{|j|}} + \langle |\zeta(\omega)|^2 \rangle, \end{aligned} \tag{36}$$

whose *central frequencies* ω_j read as

$$\begin{aligned} &\omega_0 = 0, \quad \omega_1 = -\omega_{-1} = \sqrt{\Omega_L^2 - \frac{9}{16}\omega^2_{\text{noise}}}, \\ &\omega_2 = -\omega_{-2} \approx 2\Omega_L - \frac{3}{16} \frac{\omega^2_{\text{noise}}}{\Omega_L}, \end{aligned} \tag{37}$$

and, as expected, up to negligible corrections $O(\omega^2_{\text{noise}}/\Omega_L)$ correspond to multiples of the Larmor frequency: 0, Ω_L, and $2\Omega_L$. Whereas, the *linewidths* (half-widths at half maxima) $\gamma_{|j|}$ take the form

$$\begin{aligned} &\gamma_0 \approx \Gamma_0 + \tfrac{3}{2}\omega_{\text{noise}}, \quad \gamma_1 = \Gamma_1 + \tfrac{5}{4}\omega_{\text{noise}}, \\ &\gamma_2 \approx \Gamma_2 + \tfrac{1}{2}\omega_{\text{noise}}, \end{aligned} \tag{38}$$

with Γ_i defined as in Eq. (23). All ω_j and $\gamma_{|j|}$ stated in Eqs. (37) and (38), respectively, can be determined analytically, however, we already simplified their forms above for $\omega_{\pm 2}$, γ_0, and γ_2, which are given by $\forall_j : \Omega_L \gg \Gamma_{|j|}$ and $\Omega_L \gg \omega_{\text{noise}}$.

In particular, these assumptions are guaranteed in our experiment, in which the static field B_0 is always much stronger than the noisy field B_{noise} and yields the Larmor frequency Ω_L much greater than any of the dissipation rates forming $\boldsymbol{\Gamma}$ in Eq. (23). Moreover, under these assumptions we can compute analytically also the *peak heights* $p^{a/d}_{|j|}$, which in the absorptive

case then read as

$$p_0^a = C\,\frac{27}{16}\,\omega_{\rm noise}^2\,\frac{\Gamma_0^2(2\Gamma_2+\omega_{\rm noise})}{(2\Gamma_0+3\omega_{\rm noise})^2 G(\omega_{\rm noise},\mathbf{\Gamma})}\,h(\theta), \quad (39a)$$

$$p_1^a = C\,\frac{3}{4}\,\omega_{\rm noise}\,\frac{\Gamma_0^2(2\Gamma_2+\omega_{\rm noise})}{(4\Gamma_1+5\omega_{\rm noise})\,G(\omega_{\rm noise},\mathbf{\Gamma})}\,g(\theta), \quad (39b)$$

$$p_2^a = C\,\frac{3}{32}\,\omega_{\rm noise}^2\,\frac{\Gamma_0^2}{(2\Gamma_2+\omega_{\rm noise})\,G(\omega_{\rm noise},\mathbf{\Gamma})}\,h(\theta), \quad (39c)$$

with

$$\begin{aligned} G(\omega_{\rm noise},\mathbf{\Gamma}) \coloneqq (2\Gamma_0+3\omega_{\rm noise})\big\{&3\omega_{\rm noise}^2[\Gamma_0+2(\Gamma_1+\Gamma_2)] \\ &+ 2\omega_{\rm noise}(2\Gamma_0\Gamma_1+5\Gamma_0\Gamma_1 \\ &+ 6\Gamma_1\Gamma_2)+8\Gamma_0\Gamma_1\Gamma_2\big\}, \end{aligned} \quad (40)$$

and the proportionality constant $C \coloneqq g_D^2(m_{20}^{\rm ini})^4$.

The dispersive equivalents of expressions (39) can also be determined analytically (given $\forall_j:\ \Omega_L \gg \Gamma_{|j|}$ and $\Omega_L \gg \omega_{\rm noise}$) and can be found in Appendix C. However (see Appendix C), these are negligible upon substituting the parameters applicable to our experiment. Hence, we ignore their contribution to the PSD (36) from now on.

Although Eqs. (39) allow us to predict the dependence of the peak heights for all values of noise intensity $\omega_{\rm noise}$, it directly follows that for low noise strengths they obey $p_0^a \propto \omega_{\rm noise}^2$, $p_1^a \propto \omega_{\rm noise}$, and $p_2^a \propto \omega_{\rm noise}^2$. Furthermore, their angular dependence factorizes and is given by

$$h(\theta) \coloneqq [2\,\sin(2\theta)+3\,\sin(4\theta)]^2 \quad (41)$$

for p_0^a and p_2^a, whereas for p_1^a it reads as

$$g(\theta) \coloneqq [3+2\,\cos(2\theta)+3\,\cos(4\theta)]^2. \quad (42)$$

Consistently, these angular dependencies correspond to the squares of the expressions derived in Ref. [61], when the response to a radio-frequency magnetic field is considered instead of white noise.

B. Measured noise spectra

In order to validate the theoretical model outlined above, we vary the noisy magnetic field in the table-top alignment-based magnetometer described in Sec. II C. For the purpose of experiment, we define the noise spectral density in Hz, i.e., $f_{\rm noise}$ such that $\omega_{\rm noise} = 2\pi f_{\rm noise}$. As we apply a known voltage through the coil, it is convenient to further write $f_{\rm noise} = c\,V_{\rm noise}^2$, where $V_{\rm noise}$ has units of $\rm mV_{rms}$ and the proportionality constant c can be explicitly determined for our setup (see Appendix D).

In order to measure the PSD (30) of our device, we record for a given value of $f_{\rm noise}$ 100 1-s data sets, for each of which the Fourier transform is then computed before averaging. The main plot of Fig. 3 shows an exemplary PSD obtained for the input polarization angle being set to $\theta = 40^\circ$, and a relatively low noise spectral density being applied, $f_{\rm noise} = 0.26\,\rm Hz$ (corresponding to $V_{\rm noise} = 140\,\rm mV_{rms}$). It is clear that the PSD has peaks at approximately 0, f_L, and $2f_L$ frequencies with $\Omega_L = 2\pi f_L$, as anticipated by Eq. (37).

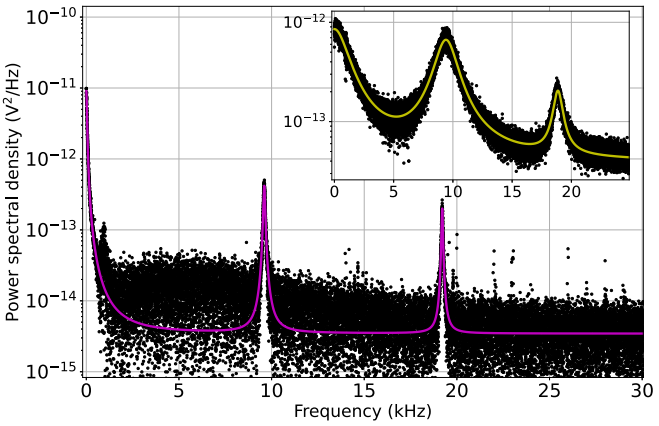

FIG. 3. Power spectral density (PSD) measured in the experiment against the theoretical fits predicted by Eq. (36). The signal was recorded over 100 time traces, each of 1 second duration. Within the main plot, relatively *low-noise* spectral density of $f_{\rm noise} = 0.26\,\rm Hz$ is chosen, corresponding to 140 $\rm mV_{rms}$ (the input polarization angle is set to $\theta = 40^\circ$). The so-obtained PSD has the experimental noise floor subtracted and is then fitted using a single function (magenta curve) containing three Lorentzian peaks with centres located close to the frequencies: $f = 0$, f_L and $2f_L$. Here, the three peaks are clearly distinguishable due to their small linewidths. In contrast, the inset shows the PSD for *high-noise* spectral density $f_{\rm noise} = 120\,\rm Hz$, corresponding to 3 $\rm V_{rms}$ (with the input polarization angle set now to $\theta = 25^\circ$), that nonetheless is well described by the same fit-function (yellow curve) despite the Lorentzian peaks now overlapping significantly.

Due to a clear separation of the peaks, the noise floor varies between them: it takes the value of approximately 6.5×10^{-14} $\rm V^2/Hz$ for the peaks centered at $f_0 = 0$ and $f_1 \approx f_L$, while it reads about 2.7×10^{-14} $\rm V^2/Hz$ for the peak at $f_2 \approx 2f_L$. When fitting the data we subtract the noise floor (data not shown) of the experiment from each data set. This removes the detection noise (and $1/f$ noise) of different strengths across the spectrum. We then fit a single function containing three Lorentzian peaks to the whole spectrum, i.e., the complete absorptive part of Eq. (36). The corresponding fit parameters obtained for each of the three peaks are listed in Table I. In contrast, when dealing with *high strengths of white noise*,

TABLE I. Fit parameters in the low-noise regime. A single function corresponding to the absorptive part of Eq. (36) is fitted to reconstruct the PSD presented in the main plot of Fig. 3. As it contains three Lorentzian profiles ($j = 0, 1, 2$), such a procedure yields three distinct sets of parameters: central frequencies (f_j), linewidths ($\widetilde{\gamma}_j$), and peak amplitudes ($\widetilde{p}_j^a$). The data were collected in the above measurement of the PSD (main plot of Fig. 3) for Larmor frequency ~9.6 kHz, the light polarization angle being set to $\theta = 40^\circ$, and the strength of applied noise set to 140 $\rm mV_{rms}$ such that $f_{\rm noise} = 0.26\,\rm Hz$.

j	f_j (Hz)	$\widetilde{\gamma}_j$ (Hz)	$\widetilde{p}_j^a$ ($\rm V^2/Hz$)
0	0	34.9(2)	$9.03(3) \times 10^{-12}$
1	9603(1)	48.6(4)	$4.16(2) \times 10^{-13}$
2	19208(1)	37.8(6)	$1.97(2) \times 10^{-13}$

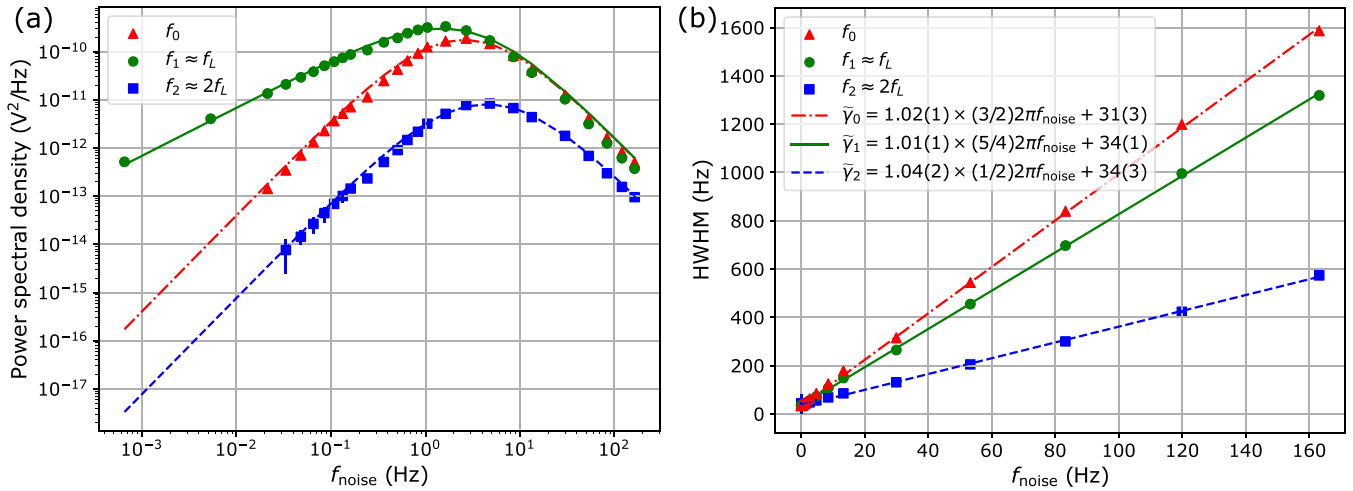

FIG. 4. Amplitudes (a) and linewidths (b) of the PSD peaks as a function of the white-noise strength, which is varied from 6.53×10^{-4} Hz to 163 Hz with the light polarization angle fixed to $\theta = 25^\circ$. For every white-noise value f_{noise}, amplitudes and linewidths are determined for each of the three relevant (absorptive) peaks in the PSD via the fitting procedure described in Fig. 3. The theoretical predictions are shown for each peak at 0 (red, dotted-dashed), $\approx f_L$ (green, solid), and $\approx 2f_L$ (blue, dashed) frequency. (a) All three peak amplitudes $\widetilde{p}_j^a$ clearly follow the theoretical predictions of Eq. (39), which we fit by tuning the overall proportionality constants [allowing different C_j for each p_j^a in Eq. (39)] and common values of the dissipation rates [Γ_0, Γ_1, and Γ_2 in Eq. (39)]. (b) The linewidths increase linearly with f_{noise} with the slope agreeing almost exactly for each peak with the proportionality constants predicted by Eq. (38). Moreover, their offsets at $f_{\text{noise}} = 0$ provide us independently with the dissipation rates [Γ_0, Γ_1, and Γ_2 appearing also in Eq. (38)], which are consistent (up to ≈ 10 Hz) with their equivalents predicted by amplitude fitting in (a) (see the main text).

the three peaks strongly overlap within the PSD, as shown explicitly for $f_{\text{noise}} = 120$ Hz within the inset of Fig. 3. As predicted by the theory, this is due to an apparent increase of the peak linewidths.

In what follows, we verify in more detail the expressions (39) for the peak amplitudes by studying explicitly their dependence on the noise spectral density f_{noise} and the light polarization angle θ.

1. Varying the noise spectral density

Figures 4(a) and 4(b) show the variation of the amplitude and linewidth, respectively, for each of the Lorentzian peaks fitted around $f = 0$, f_L, and $2f_L$, as a function of the noise spectral density f_{noise} (in Hz). The data were collected with a fixed, $\theta = 25^\circ$, polarization angle of the input beam. As described above, the fitting procedure was done using a single fitting function. The applied voltage to generate the noisy magnetic field was varied from 7 mV_{rms} to 3500 mV_{rms}. To convert this to spectral density (in Hz) we determine the proportionality constant in $f_{\text{noise}} = c\text{V}_{\text{noise}}^2$ as $c = 1.33(3) \times 10^{-5}$ $\text{Hz/mV}_{\text{rms}}^2$, which is possible via the calibration procedure described in Appendix D.

Crucially, the experimental results are consistent with the theory, in particular, the amplitudes of the three (absorptive) peaks follow the functional dependencies predicted by Eq. (39), with, e.g., quadratic and linear dependencies: $\widetilde{p}_0^a \propto f_{\text{noise}}^2$, $\widetilde{p}_1^a \propto f_{\text{noise}}$, and $\widetilde{p}_2^a \propto f_{\text{noise}}^2$, easily verifiable from Fig. 4(a) in the low white-noise regime. Performing the full fitting procedure, we allow the proportionality constants in Eq. (39) to differ (C_j for each p_j^a), while determining common dissipation rates that are most consistent with the data (Γ_0, Γ_1, and Γ_2). We obtain $C_0 = 2.1(2) \times 10^{-6}$ V^2, $C_1 = 3.4(6) \times 10^{-6}$ V^2, and $C_2 = 1.0(1) \times 10^{-6}$ V^2 for each peak, respectively, which consistently are of the same order, whereas the best-fitted dissipation rates read as $\widetilde{\Gamma}_0 = 29(1)$ Hz, $\widetilde{\Gamma}_1 = 43(4)$ Hz, and $\widetilde{\Gamma}_2 = 29(2)$ Hz. On the other hand, the corresponding linewidths depicted in Fig. 4(b) follow linear dependencies in f_{noise} with the slope almost identical to the proportionality constants predicted by Eq. (38). Moreover, their offsets at f_{noise} allow us to independently determine the dissipation rates (23) as $\widetilde{\Gamma}_0 = 31(3)$ Hz, $\widetilde{\Gamma}_1 = 34(1)$ Hz, and $\widetilde{\Gamma}_2 = 34(3)$ Hz. These are in a good agreement (within ≈ 10 Hz) with the ones found when fitting the three peak amplitudes in Fig. 4(a).

Last but not least, let us comment on the ability of our theoretical models to predict changes in the central frequencies of the peaks. Figure 5 shows how the central frequency, for the peak around f_L (green dots) and $2f_L$ (blue squares), vary as a function of the noise spectral density in the experiment. The theoretically predicted relation (37) is then fit to the experimental data (dashed lines) with $f_L = \Omega_L/(2\pi) = 9435(1)$ Hz being the only free parameter. It can be seen that the theory agrees reasonably well with the experimental data with the central frequency slightly decreasing in the high noise regime for the peak at f_L and remaining almost the same for the second peak. Note that the error on the values for the central frequencies are within ± 5 Hz. These errors come from experimental imperfections, however, such as the central frequency drifting in the time it takes for all of the data to be taken, and errors in fitting the data. It is noted here that the errors in fitting the central frequency at $2f_L$ will be larger than at f_L due to the peaks being at least an order of magnitude smaller and hence closer to the noise floor of the experiment. Bearing in mind all the aforementioned imperfections, one may conclude that theory predicts well the

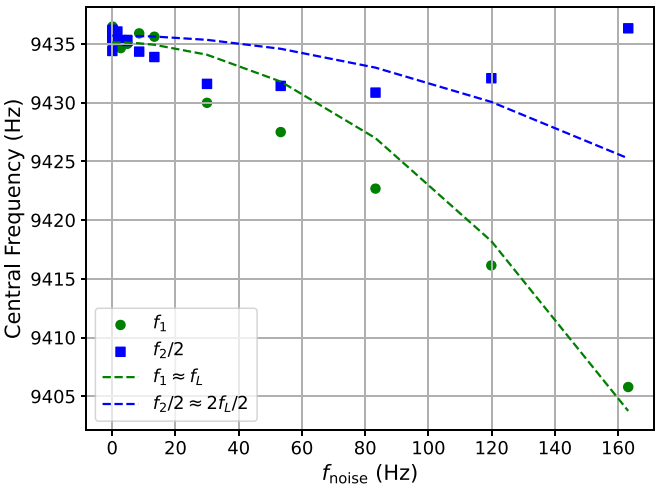

FIG. 5. Central frequency of the PSD peaks as a function of the noise spectral density (f_{noise}), which is varied from 6.53×10^{-4} to 163 Hz with the light polarization angle being fixed to $\theta = 25^\circ$. The theoretical predictions of the change in central frequency [Eq. (37)] are shown over the full range of the noise spectral densities applied (dashed lines) with $f_L = 9435(1)$ Hz fitted to the experimental data for $f_1 \approx f_L$ (green dots) and $f_2 \approx 2f_L$ (blue squares). The overall error in the experimentally determined central frequencies is approximately ± 5 Hz, arising both from experimental imperfections (e.g., drifts, background-noise subtraction) and the fitting procedure.

dependence of the central frequencies on the noise density for both peaks.

2. *Varying the light polarization angle*

Finally, as the angular dependence of the peak amplitudes (39) separates from all other parameters in the form of functions $h[\theta]$ and $g[\theta]$ stated in Eqs. (41) and (42), we verify this explicitly in the low white-noise regime with $V_{\text{noise}} = 140\ \text{mV}_{\text{rms}}$, corresponding to $f_{\text{noise}} = 0.26$ Hz, by varying the polarization angle of the incoming light from $\theta = -20^\circ$ to 120°. It is noted that the Larmor frequency used for varying the polarization angle was ~9.6 kHz. The results are presented in Fig. 6 with measurements reproducing almost exactly the predicted angular behaviors. As the linewidths of the peaks do not vary significantly when varying θ (data not shown), we may use the values $\widetilde{\gamma}_j$ determined for this low value of noise in Fig. 4(a) and compute separately the exact proportionality constants for each $\widetilde{p}_j^{\alpha}$ such that the functions $h[\theta]$ and $g[\theta]$ are most accurately reproduced. In this way, while accounting also for a common angular offset $\theta \to \theta + \delta\theta$ with $\delta\theta = 0.77(7)^\circ$ in our setup, we obtain $C_0 = 3.9(6) \times 10^{-6}$ V, $C_1 = 2.1(1) \times 10^{-6}$ V, and $C_2 = 1.5(4) \times 10^{-6}$ V, which are consistently of similar magnitude and almost the same as the ones determined above when varying the white-noise strength.

IV. CONCLUSIONS

We prepare a detailed dynamical model allowing us to predict spin noise spectra of an alignment-based magnetometer, which we then verify experimentally. Its applicability relies on the presence of the excess white noise being applied along the propagation direction of the light beam that is used to both

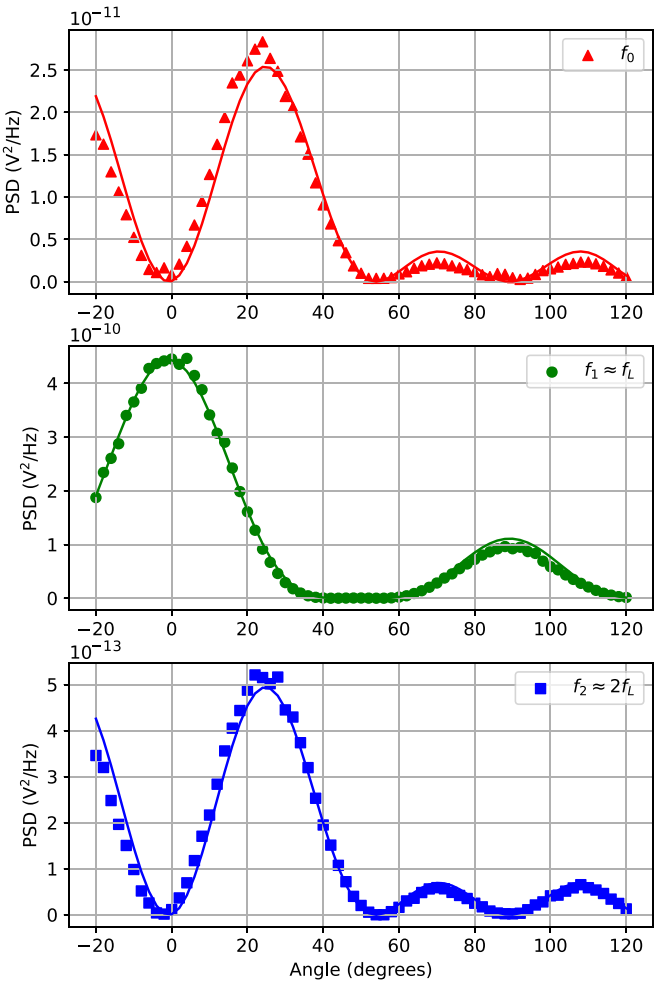

FIG. 6. Amplitudes of the PSD peaks as a function of the light polarization angle, which is varied from $\theta = -20^\circ$ to 120° with the white-noise strength set to $V_{\text{noise}} = 140\ \text{mV}_{\text{rms}}$, corresponding to $f_{\text{noise}} = 0.26$ Hz. The fits predicted theoretically by Eq. (39), in particular, the angular dependencies $h[\theta]$ and $g[\theta]$ stated in Eqs. (41) and (42), are shown as solid curves for the peaks centered around frequencies 0 (red), f_L (green), and $2f_L$ (blue).

pump and probe the atomic ensemble, which is perpendicular to the direction of the strong magnetic field responsible for Larmor precession.

On the one hand, the added noise amplifies the Larmor-induced peaks to be clearly visible within the power spectral density above the level of detection noise. As a result, our model describing the spin noise in the device can now be used by signal-processing tools to interpret the detection data better, e.g., when operating the device as a scalar magnetometer, Bayesian inference methods such as the Kalman filter [48] can be applied to track fast changes of the strong magnetic field in real time beyond the magnetometer bandwidth [62,63]. On the other hand, the induced noise can be used to naturally perform sensing tasks in the so-called *covert* manner [64], i.e., so that an adversary having access to the output of the magnetometer would not be able to recover the signal without possessing the precalibrated dynamical model that we propose. In this sense, we expect our model to be useful also for tracking time-varying signals encoded in oscillating RF fields (amplitude

and phase) directed perpendicularly to both the scalar field and the added noise.

It would be interesting to generalize our model to a device that operates at the quantum limit [35–37], i.e., with detection noise being small enough, so that the predicted peaks in the spectrum arise without the need to artificially amplify them by applying the excess classical noise. Moreover, similarly to orientation-based magnetometers [38,52,65], maybe such model could be also capable to incorporate the effect of pumping and probing the ensemble with squeezed light, so the detection noise can be even further reduced. We leave such open questions for the future.

Experimental data created during this research are openly available from The University of Nottingham data repository [66].

ACKNOWLEDGMENTS

This work was supported by the QuantERA grant C'MON-QSENS! funded by the Engineering and Physical Sciences Research Council (EPSRC) (Grant No. EP/T027126/1). Project C'MON-QSENS! is also supported by the National Science Centre (2019/32/Z/ST2/00026), Poland, under QuantERA, which has received funding from the European Union's Horizon 2020 research and innovation programme under Grant Agreement No. 731473. The work was also supported by the Novo Nordisk Foundation (Grant No. NNF20OC0064182) and the UK Quantum Technology Hub in Sensing and Timing, funded EPSRC (Grant No. EP/T001046/1) and EPSRC Grant No. EP/Y005260/1.

APPENDIX A: EVOLUTION IN THE BASIS OF SPHERICAL-TENSOR OPERATORS

The evolution of the atomic ensemble without the effect of pumping, described by Eq. (19), is written in terms of the density matrix (1). In this Appendix we show how to write it in terms of the vector of all spherical-tensor components $\mathbf{m}_t^{\text{full}}$. In particular, since the right-hand side of the equation is linear in terms of ρ, we would like to find specific linear operators that act on $\mathbf{m}_t^{\text{full}}$ that correspond to specific operations performed on ρ, and enable us to write the dynamical equation in the form of (21). We also show that, since the resulting operators do not couple spherical-tensor components of different rank, we only need the rank-2 component for a full description of the problem under consideration.

1. Rotations induced by magnetic fields

Spherical-tensor operators $\mathcal{T}_q^{(\kappa)}$ are defined by the decomposition of the density matrix (1) with respect to irreducible representations of the three-dimensional rotation group, i.e., for each $\kappa = 0, \ldots, 2F$, operators $\mathcal{T}_q^{(\kappa)}$ with $q = -\kappa, \ldots, \kappa$ form a basis of a $(2\kappa+1)$-dimensional irreducible representation. These operators form a convenient basis for density matrices of a system with fixed angular momentum F:

$$\rho = \sum_{\kappa=0}^{2F} \sum_{q=-\kappa}^{\kappa} m_{\kappa q} \mathcal{T}_q^{(\kappa)}, \tag{A1}$$

with a scalar product $\mathrm{Tr}[\mathcal{T}_q^{(\kappa)\dagger} \mathcal{T}_{q'}^{(\kappa')}] = \delta_{\kappa\kappa'}\delta_{qq'}$, and with well-defined behavior under rotations generated by the angular-momentum operators, i.e., a vector $\hat{\boldsymbol{F}} := (\hat{F}_x, \hat{F}_y, \hat{F}_z)^T$. In particular, any SO(3) rotation can be parametrized either by the axis (represented by a normalized vector $\boldsymbol{n}$), and angle of rotation φ:

$$\hat{\mathcal{R}}(\boldsymbol{n}, \varphi) = e^{-i\varphi \boldsymbol{n}\cdot\hat{\boldsymbol{F}}}, \tag{A2}$$

or by the three Euler angles ϕ, θ, ψ that correspond to subsequent rotations about the z, y, and again the z axes, respectively:

$$\hat{\mathcal{R}}(\psi, \theta, \phi) = e^{-i\psi \hat{F}_z} e^{-i\theta \hat{F}_y} e^{-i\phi \hat{F}_z}. \tag{A3}$$

We now use the operator above to define the Wigner D-matrix:

$$D^{(F)}_{M,M'}(\psi, \theta, \phi) := \langle F, M | \hat{\mathcal{R}}(\psi, \theta, \phi) | F, M' \rangle. \tag{A4}$$

The spherical-tensor operators behave analogously to angular-momentum eigenstates under rotations if we treat the rank κ as the total angular momentum, and the index q as the projection on the z axis:

$$\hat{\mathcal{R}}(\psi, \theta, \phi) \mathcal{T}_{q'}^{(\kappa)} \hat{\mathcal{R}}(\psi, \theta, \phi)^\dagger = \sum_{q=-\kappa}^{\kappa} D^{(\kappa)}_{q,q'}(\psi, \theta, \phi) \mathcal{T}_q^{(\kappa)}. \tag{A5}$$

This means that for the spherical-tensor component vector $\mathbf{m}_t^{(\kappa)}$ composed of $m_{\kappa,q}(t)$ coefficients ($q = -\kappa, \ldots, \kappa$), the rotation generators are $\mathbf{J}_x^{(\kappa)}$, $\mathbf{J}_y^{(\kappa)}$, and $\mathbf{J}_z^{(\kappa)}$, which are the matrix representations of angular momentum operators cut to the subspace of total angular momentum κ.

This simplifies the study of dynamics of ρ under rotations, but also facilitates the description of light-atom interactions. Whenever one considers dipole-type interactions, which correspond to multiplying two (dipole) vectors, spherical-tensor components with $\kappa \leqslant 2$ describing the atom are sufficient to find the output light state [26,57].

We use these properties of the spherical tensor to find the expressions for the evolution of the atomic state described by Eq. (19) in the spherical-tensor basis. Since the Hamiltonian resulting from the magnetic field generates the rotation of the atomic state about the magnetic field vector $\boldsymbol{B}$,

$$\frac{d\rho}{dt} = -i[\gamma_{\text{gmr}} \boldsymbol{B} \cdot \hat{\boldsymbol{F}}, \rho], \tag{A6}$$

the evolution in the spherical-tensor basis will also be driven by respective rotation generators

$$\frac{d\mathbf{m}_t^{(\kappa)}}{dt} = -i\gamma_{\text{gmr}} (\boldsymbol{B} \cdot \boldsymbol{J}^{(\kappa)}) \mathbf{m}_t^{(\kappa)}, \tag{A7}$$

where $\boldsymbol{J}^{(\kappa)} = (\mathbf{J}_x^{(\kappa)}, \mathbf{J}_y^{(\kappa)}, \mathbf{J}_z^{(\kappa)})^{\mathrm{T}}$.

This can be directly shown using the commutation relations for the spherical-tensor operators and the angular-momentum operators:

$$\left[\hat{F}_z, \mathcal{T}_q^{(\kappa)}\right] = \hbar q \mathcal{T}_q^{(\kappa)}, \tag{A8}$$

$$\left[\hat{F}_\pm, \mathcal{T}_q^{(\kappa)}\right] = \hbar \sqrt{\kappa(\kappa+1) - q(q\pm 1)} \mathcal{T}_{\pm q}^{(\kappa)}, \tag{A9}$$

that enable us to find the exact form of the matrix:

$$\begin{aligned} (\mathbf{A}_0)^{(\kappa),q}_{(\kappa'),q'} &= -\frac{i\Omega_L}{\hbar} \mathrm{tr}\left\{\mathcal{T}_q^{(\kappa)\dagger}\left[\hat{F}_z, \mathcal{T}_{q'}^{(\kappa')}\right]\right\} \\ &= -i\Omega_L q \delta_{\kappa\kappa'}\delta_{qq'} = -i\Omega_L \left(\mathbf{J}_z^{(\kappa)}\right)^q_{q'}. \end{aligned} \tag{A10}$$

Using Eq. (A9) we could analogously find that commuting the density matrix with $\hat{F}_x$ and $\hat{F}_y$ is equivalent to acting the operators $\mathbf{J}_x^{(\kappa)}$ and $\mathbf{J}_y^{(\kappa)}$, respectively, on $\mathbf{m}_t^{(\kappa)}$. We use this to also obtain

$$\mathbf{A}_{\text{noise}} = -i\sqrt{\omega_{\text{noise}}}\mathbf{J}_x^{(2)}. \tag{A11}$$

Let us now note that commuting density matrix twice with some operator

$$[\hat{F}_\alpha, [\hat{F}_\alpha, \rho]] = 2\hat{F}_\alpha\rho\hat{F}_\alpha - \{\hat{F}_\alpha^2, \rho\} \tag{A12}$$

is then equivalent to acting with the square of the respective operator $\mathbf{J}_\alpha^{(\kappa)}$. This is responsible for the appearance of the $\mathbf{A}_{\text{noise}}^2/2$ term in Eq. (21). In either case, the operation does not couple spherical-tensor coefficients of different rank.

2. Decoherence

We would also like to find the correct description of decoherence using the spherical-tensor coefficients. It is driven by nonunitary evolution, described by an operator

$$\frac{d\rho}{dt} = \Phi[\rho] = \sum_\alpha \Phi_\alpha[\rho] + \Phi_{\text{iso}}[\rho], \tag{A13}$$

where $\Phi_\alpha[\rho]$ is the part of dissipation that comes from the unknown fluctuations of the magnetic field:

$$\Phi_\alpha[\rho] = \Gamma_\alpha\big(\hat{F}_\alpha\rho\hat{F}_\alpha - \tfrac{1}{2}\{\hat{F}_\alpha^2, \rho\}\big), \tag{A14}$$

and the isotropic part of the dissipation reads as

$$\Phi_{\text{iso}}[\rho] = \Lambda - \tfrac{1}{2}\{\hat{\Gamma}, \rho\}, \tag{A15}$$

where $\hat{\Gamma} = \Gamma_{\text{iso}}\mathbb{1}_{2F+1}$ and $\Lambda = \frac{\Gamma_{\text{iso}}}{2F+1}\mathbb{1}_{2F+1}$. It causes the decay of all matrix components at the same rate Γ_{iso} $(-\frac{1}{2}\{\hat{\Gamma}, \rho\})$ and pumps the $m_{0,0}$ components in the rate that balances the decay (Λ). This means that all of the $\kappa \neq 0$ components of the spherical tensor decay at the same rate Γ_{iso}:

$$\frac{dm_{\kappa,q}}{dt} = -\Gamma_{\text{iso}}m_{\kappa,q}. \tag{A16}$$

The operator (A14), on the other hand, is proportional to a double commutator of Eq. (A12), therefore, we obtain the following operator of decoherence in the spherical-tensor basis:

$$\mathbf{A}_\Phi = -\frac{1}{2}\sum_\alpha \Gamma_\alpha\big(\mathbf{J}_\alpha^{(2)}\big)^2 - \Gamma_{\text{iso}}\mathbb{1}_5, \tag{A17}$$

which for the case $\Gamma_x = \Gamma_y = \Gamma_\perp$, $\Gamma_z = \Gamma_\parallel$ takes the form

$$\mathbf{A}_\Phi = -\begin{pmatrix} \Gamma_2 & 0 & 0 & 0 & 0 \\ 0 & \Gamma_1 & 0 & 0 & 0 \\ 0 & 0 & \Gamma_0 & 0 & 0 \\ 0 & 0 & 0 & \Gamma_1 & 0 \\ 0 & 0 & 0 & 0 & \Gamma_2 \end{pmatrix}, \tag{A18}$$

with

$$\Gamma_0 = 3\Gamma_\perp + \Gamma_{\text{iso}}, \tag{A19}$$

$$\Gamma_1 = \tfrac{1}{2}(\Gamma_\parallel + 5\Gamma_\perp) + \Gamma_{\text{iso}}, \tag{A20}$$

$$\Gamma_2 = 2\Gamma_\parallel + \Gamma_\perp + \Gamma_{\text{iso}}. \tag{A21}$$

We see again that spherical-tensor coefficients of different rank do not couple, so we can limit our considerations to the rank-2 component, relevant to our physical system.

APPENDIX B: NOISE SPECTRUM RESULTING FROM AN INHOMOGENEOUS LINEAR SDE

For the purpose of predicting the spin noise spectrum, we need to consider the following multiple-variable stochastic differential equation:

$$d\mathbf{m}_t = (\mathbf{v} + \mathbf{F}\mathbf{m}_t)dt + \mathbf{G}\mathbf{m}_t\, dW_t, \tag{B1}$$

where $\mathbf{m}_t$ is an evolving vector, while operators $\mathbf{F}$ and $\mathbf{G}$ together with vector $\mathbf{v}$ parametrize the evolution of the system. The equation is linear and inhomogeneous. Equations like this, in general, are not analytically solvable if the operators $\mathbf{F}$ and $\mathbf{G}$ do not commute. However, we only need to calculate the Fourier transform of the time-autocovariance matrix:

$$\boldsymbol{\Xi}(t) = \big\langle \mathbf{m}_0, \mathbf{m}_t^{\mathrm{T}} \big\rangle_{\text{ss}} = \big\langle \mathbf{m}_0\mathbf{m}_t^{\mathrm{T}} \big\rangle_{\text{ss}} - \langle \mathbf{m}_0 \rangle_{\text{ss}} \big\langle \mathbf{m}_t^{\mathrm{T}} \big\rangle_{\text{ss}}. \tag{B2}$$

In order to obtain the steady-state mean value $\langle \dots \rangle_{\text{ss}}$, we average over the possible paths of the stochastic process W_t given particular value of the initial point $\mathbf{m}_0$, and then separately over all values of the initial point. We indicate these subsequent stochastic averages explicitly by the distinct subscripts, i.e.,

$$\big\langle \mathbf{m}_0\mathbf{m}_t^{\mathrm{T}} \big\rangle_{\text{ss}} = \big\langle \mathbf{m}_0 \big\langle \mathbf{m}_t^{\mathrm{T}} \big\rangle_{W_t|\mathbf{m}_0} \big\rangle_{\mathbf{m}_0}. \tag{B3}$$

Path averaging of Eq. (B1), which cancels the stochasic increment, leads to

$$\frac{d}{dt}\langle \mathbf{m}_t \rangle_{W_t|\mathbf{m}_0} = \mathbf{v} + \mathbf{F}\langle \mathbf{m}_t \rangle_{W_t|\mathbf{m}_0}, \tag{B4}$$

which yields the following evolution of the average value:

$$\langle \mathbf{m}_t \rangle_{W_t} = -\mathbf{F}^{-1}\mathbf{v} + e^{\mathbf{F}t}(\mathbf{m}_0 + \mathbf{F}^{-1}\mathbf{v}). \tag{B5}$$

The steady-state mean of $\mathbf{m}_t$, which is only obtained if all eigenvalues of $\mathbf{F}$ have negative real parts, can be found by taking the limit $t \to +\infty$:

$$\langle \mathbf{m} \rangle_{\text{ss}} = -\mathbf{F}^{-1}\mathbf{v}, \tag{B6}$$

where we drop the subscript t in $\mathbf{m}$ because by definition the steady-state mean value does not evolve.

Finally, by substituting the expressions (B5) and (B6) into Eq. (B2) we obtain

$$\big\langle \mathbf{m}_0, \mathbf{m}_t^{\mathrm{T}} \big\rangle_{\text{ss}} = [\langle \mathbf{m}\mathbf{m}^{\mathrm{T}} \rangle_{\text{ss}} - \mathbf{F}^{-1}\mathbf{v}\mathbf{v}^{\mathrm{T}}(\mathbf{F}^{-1})^{\mathrm{T}}]e^{\mathbf{F}^{\mathrm{T}}t}, \tag{B7}$$

which is true for $t \geqslant 0$. An analogous result for $t < 0$ can be found by the use of the fact that for the steady state

$$\big\langle \mathbf{m}_0, \mathbf{m}_{-t}^{\mathrm{T}} \big\rangle_{\text{ss}} = \big\langle \mathbf{m}_t, \mathbf{m}_0^{\mathrm{T}} \big\rangle_{\text{ss}} = \big\langle \mathbf{m}_0, \mathbf{m}_t^{\mathrm{T}} \big\rangle^{\mathrm{T}}, \tag{B8}$$

so that for any t we can finally write

$$\big\langle \mathbf{m}_0, \mathbf{m}_t^{\mathrm{T}} \big\rangle_{\text{ss}} = \begin{cases} [\langle \mathbf{m}\mathbf{m}^{\mathrm{T}} \rangle_{\text{ss}} - \mathbf{F}^{-1}\mathbf{v}\mathbf{v}^{\mathrm{T}}(\mathbf{F}^{-1})^{\mathrm{T}}]e^{\mathbf{F}^{\mathrm{T}}t} & \text{for } t < 0, \\ e^{-\mathbf{F}^{\mathrm{T}}t}[\langle \mathbf{m}\mathbf{m}^{\mathrm{T}} \rangle_{\text{ss}} - \mathbf{F}^{-1}\mathbf{v}\mathbf{v}^{\mathrm{T}}(\mathbf{F}^{-1})^{\mathrm{T}}] & \text{for } t \geqslant 0. \end{cases} \tag{B9}$$

In order to get the mean steady-state value of $\langle \mathbf{m}\mathbf{m}^{\mathrm{T}} \rangle$, we need to find

$$d(\mathbf{m}_t\mathbf{m}_t^{\mathrm{T}}) = d\mathbf{m}_t\, \mathbf{m}_t^{\mathrm{T}} + \mathbf{m}_t\, d\mathbf{m}_t^{\mathrm{T}} + d\mathbf{m}_t\, d\mathbf{m}_t^{\mathrm{T}}. \tag{B10}$$

The $d\mathbf{m}_t\, d\mathbf{m}_t^{\mathrm{T}}$ term is necessary to account for the property of the stochastic increment that $dW_t^2 = dt$. We substitute $d\mathbf{m}_t$ from Eq. (B1), take the average, divide by dt, and obtain

$$\frac{d}{dt}\langle \mathbf{m}_t \mathbf{m}_t^{\mathrm{T}}\rangle = \mathbf{v}\langle \mathbf{m}_t^{\mathrm{T}}\rangle + \langle \mathbf{m}_t\rangle \mathbf{v}^{\mathrm{T}} + \mathbf{F}\langle \mathbf{m}_t \mathbf{m}_t^{\mathrm{T}}\rangle + \langle \mathbf{m}_t \mathbf{m}_t^{\mathrm{T}}\rangle \mathbf{F}^{\mathrm{T}} + \mathbf{G}\langle \mathbf{m}_t \mathbf{m}_t^{\mathrm{T}}\rangle \mathbf{G}^{\mathrm{T}}, \tag{B11}$$

which equals 0 in the steady state. Hence, after substituting $\langle \mathbf{m}_t\rangle = \langle \mathbf{m}\rangle_{\mathrm{ss}}$ from (B6), we obtain

$$\mathbf{F}\,\boldsymbol{\sigma} + \boldsymbol{\sigma}\,\mathbf{F}^{\mathrm{T}} + \mathbf{G}\,\boldsymbol{\sigma}\,\mathbf{G}^{\mathrm{T}} = \mathbf{v}\,\mathbf{v}^{\mathrm{T}}\,(\mathbf{F}^{\mathrm{T}})^{-1} + \mathbf{F}^{-1}\,\mathbf{v}\,\mathbf{v}^{\mathrm{T}}, \tag{B12}$$

where $\boldsymbol{\sigma} = \langle \mathbf{m}\,\mathbf{m}^{\mathrm{T}}\rangle_{\mathrm{ss}}$. Importantly, in case we are given a specific set of $\mathbf{v}$, $\mathbf{F}$, and $\mathbf{G}$, we can solve (B12) as a system of linear equations to find $\boldsymbol{\sigma}$.

Possessing a particular form of $\boldsymbol{\sigma}$, we can explicitly calculate the Fourier transform of $\boldsymbol{\Xi}(t)$, i.e.,

$$\boldsymbol{\Xi}(\omega) = \int_{-\infty}^{0} dt\, e^{-\mathbf{F}^{\mathrm{T}} t}[\langle \mathbf{m}\mathbf{m}^{\mathrm{T}}\rangle - \mathbf{F}^{-1}\mathbf{v}\mathbf{v}^{\mathrm{T}}(\mathbf{F}^{-1})^{\mathrm{T}}] + \int_{0}^{+\infty} dt[\boldsymbol{\sigma} - \mathbf{F}^{-1}\mathbf{v}\mathbf{v}^{\mathrm{T}}(\mathbf{F}^{\mathrm{T}})^{-1}]\exp[(-i\omega + \mathbf{F}^{\mathrm{T}})t] \tag{B13}$$

$$= -\frac{1}{2\pi}(\mathbf{F} + i\omega)^{-1}[\boldsymbol{\sigma} - \mathbf{F}^{-1}\mathbf{v}\mathbf{v}^{\mathrm{T}}(\mathbf{F}^{\mathrm{T}})^{-1}] - \frac{1}{2\pi}[\boldsymbol{\sigma} - \mathbf{F}^{-1}\mathbf{v}\mathbf{v}^{\mathrm{T}}(\mathbf{F}^{\mathrm{T}})^{-1}](\mathbf{F}^{\mathrm{T}} - i\omega)^{-1}. \tag{B14}$$

We can simplify this formula by using Eq. (B12) and finding that

$$(\mathbf{F} + i\omega)\boldsymbol{\Xi}(\omega)(\mathbf{F}^{\mathrm{T}} - i\omega) = \mathbf{G}\,\boldsymbol{\sigma}\,\mathbf{G}^{\mathrm{T}}, \tag{B15}$$

so we obtain

$$\boldsymbol{\Xi}(\omega) = (\mathbf{F} + i\omega)^{-1}\mathbf{G}\,\boldsymbol{\sigma}\,\mathbf{G}^{\mathrm{T}}(\mathbf{F}^{\mathrm{T}} - i\omega)^{-1}. \tag{B16}$$

If the signal is a linear combination of the $\mathbf{m}_t$ components, parametrized by a vector $\mathbf{k}$ of the same dimension as $\mathbf{m}_t$:,

$$S(t) = \mathbf{k}^{\mathrm{T}}\,\mathbf{x}_t, \tag{B17}$$

then the PSD is given by

$$\mathrm{PSD}(\omega) = \mathbf{k}^{\mathrm{T}}\,\boldsymbol{\Xi}(\omega)\,\mathbf{k} = \mathbf{k}^{\mathrm{T}}\,(\mathbf{F} + i\omega)^{-1}\mathbf{G}\,\boldsymbol{\sigma}\,\mathbf{G}^{\mathrm{T}}(\mathbf{F}^{\mathrm{T}} - i\omega)^{-1}\,\mathbf{k}. \tag{B18}$$

Effective Lorentzian form

To find the functional form of $\mathrm{PSD}(\omega)$ one can write Eq. (B18) in the eigenbasis of the $\mathbf{F}$ matrix. If we write the eigenvalues of $\mathbf{F}$ as $\lambda_\alpha = -\gamma_\alpha + i\omega_\alpha$, then

$$\mathrm{PSD}(\omega) = \sum_{\alpha,\beta}\frac{k_\alpha k_\beta Q_{\alpha\beta}}{[-\gamma_\alpha + i(\omega+\omega_\alpha)][-\gamma_\beta - i(\omega-\omega_\beta)]} = \sum_{\alpha,\beta} k_\alpha k_\beta Q_{\alpha\beta}\frac{\gamma_\alpha+\gamma_\beta+i(\omega_\alpha+\omega_\beta)}{(\gamma_\alpha+\gamma_\beta)^2+(\omega_\alpha+\omega_\beta)^2} \times\left(\frac{\gamma_\alpha + i(\omega+\omega_\alpha)}{\gamma_\alpha^2+(\omega+\omega_\alpha)^2} + \frac{\gamma_\beta - i(\omega-\omega_\beta)}{\gamma_\beta^2+(\omega-\omega_\beta)^2}\right), \tag{B19}$$

where k_α, k_β are the components of the $\mathbf{k}$ vector and $Q_{\alpha\beta}$ are the components of the matrix $\mathbf{G}\,\boldsymbol{\sigma}\,\mathbf{G}^{\mathrm{T}}$, in both cases written in the eigenbasis of $\mathbf{F}$. As one can see, the resulting spectrum is a sum of symmetric (absorptive) and antisymmetric (dispersive) Lorentzian peaks, whose widths are the opposites of real parts (γ_α), and central frequencies are the imaginary parts of the eigenvalues and their opposites ($\pm\omega_\alpha$):

$$\mathrm{PSD}(\omega) = \sum_{\alpha}\left(\frac{p_\alpha^a\gamma_\alpha^2}{\gamma_\alpha^2+(\omega-\omega_\alpha)^2} + \frac{p_\alpha^a\gamma_\alpha^2}{\gamma_\alpha^2+(\omega+\omega_\alpha)^2} + \frac{p_\alpha^d\gamma_\alpha(\omega-\omega_\alpha)}{\gamma_\alpha^2+(\omega-\omega_\alpha)^2} + \frac{p_\alpha^d\gamma_\alpha(\omega+\omega_\alpha)}{\gamma_\alpha^2+(\omega+\omega_\alpha)^2}\right), \tag{B20}$$

which, in the case of a real signal $S(t)$ we know to be real, positive, and symmetric around $\omega = 0$.

APPENDIX C: ANALYTIC PREDICTION OF PEAK AMPLITUDES

Crucially, the atomic magnetometer under study, described by dynamics (24), constitutes an example of stochastic inhomogeneous evolution discussed in Appendix B, so that the PSD without external noise $\zeta(t)$ is given by Eq. (B18) with $\mathbf{v} = \mathbf{A}_\Phi\mathbf{m}^{\mathrm{ss}}$, $\mathbf{F} = \mathbf{A}_0 + \mathbf{A}_\Phi + \frac{\mathbf{A}_{\mathrm{noise}}^2}{2}$, $\mathbf{G} = \mathbf{A}_{\mathrm{noise}}$, and $\mathbf{k} = \mathbf{D}_\theta^{(2)\mathrm{T}}\,\mathbf{h}$.

Since the characteristic polynomial of the matrix $\mathbf{F}$ has real coefficients, we know that it has at least one real eigenvalue, while the other two are, in pairs, complex conjugates of each other. This limits the number and character of peaks to one symmetric peak at zero, and two pairs of peaks of opposite frequencies, that are sums of symmetric and antisymmetric peaks:

$$\mathrm{PSD}(\omega) = \sum_{j=-2,\ldots,2}\frac{p_{|j|}^a\gamma_{|j|}^2}{(\omega-\omega_j)^2+\gamma_{|j|}^2} \tag{C1}$$

$$+ \sum_{j=\pm1,\pm2}\frac{\pm p_{|j|}^d\gamma_{|j|}(\omega-\omega_j)}{(\omega-\omega_j)^2+\gamma_{|j|}^2}, \tag{C2}$$

where the approximate ω_j and γ_j are given by Eqs. (37) and (38) of main text, respectively.

The formula resulting from Eq. (B18) has a complex form, practically only possible to obtain and store using symbolic calculation software, therefore, it does not provide a clear picture of the properties of the spectrum, except for making it possible to plot it numerically. In order to find the specific values of p_i^a, p_i^d, which are hidden in the formula, we use the observation that for $\Omega_L \gg \gamma_i$ the heights of the peaks in the spectrum do not depend on Ω_L, and therefore the limits

$$p_i^a \approx \lim_{\Omega_L\to+\infty}\mathrm{PSD}(\omega=\omega_i) \tag{C3}$$

will give, in sufficiently good approximation, the values of p_i^a. To obtain the approximate values of p_i^d, we calculate

$$p_i^d \approx \frac{\Gamma_i}{\Omega_L}\lim_{\Omega_L\to+\infty}\left(\Omega_L\frac{d}{d\omega}\mathrm{PSD}(\omega)\Big|_{\omega=\omega_i}\right) \tag{C4}$$

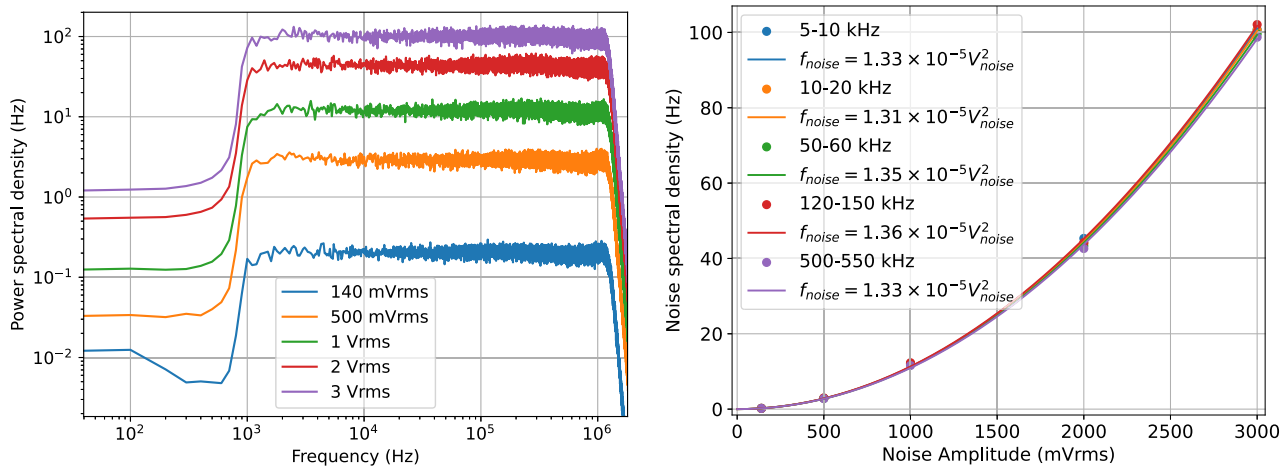

FIG. 7. Amplitude calibration for the noise spectral density $\omega_{\text{noise}} = 2\pi f_{\text{noise}}$. (a) The output current of the noise generator is first transmitted through both 1-kHz high-pass and 1-MHz low-pass filters, before being directly measured. 100 independent time traces of 0.01-s duration (sampled at a rate 40 MHz) are recorded to compute the resulting *power spectral density* (PSD) shown, which is converted into the units of Hz after accounting for the calibration factor of the coil inducing the noisy magnetic field and the gyromagnetic ratio of caesium. (b) In order to obtain the effective magnitude of the PSD, i.e., the *noise spectral density*, the average value of the PSD is computed for five different frequency ranges, as a function of the amplitude V_{noise} of the noise applied. The plot shows quadratic fits $f_{\text{noise}} = cV^2_{\text{noise}}$, applicable to each of the five frequency ranges used for averaging. All these agree and yield $c = 1.33(3) \times 10^{-5}$ Hz/mV$^2_{\text{rms}}$.

because we need the second order of expansion in $\frac{1}{\Omega_L}$. Using this approximation we obtain Eqs. (39) from the main text, and

$$p_1^d = g_D^2 \frac{3}{2} \left(m_{20}^{\text{ini}}\right)^4 \frac{\omega_{\text{noise}}}{\Omega_L} \frac{\Gamma_0^2 \left[16\Gamma_1^2\Gamma_2 + 8\Gamma_1(\Gamma_1 + 5\Gamma_2)\omega_{\text{noise}} + 16(\Gamma_1 + \Gamma_2)\omega_{\text{noise}}^2 + 3\omega_{\text{noise}}^3\right]}{(4\Gamma_1 + 5\omega_{\text{noise}})^3 \, G(\omega_{\text{noise}}, \mathbf{\Gamma})} [3 + 2\cos(2\theta) + 3\cos(4\theta)]^2, \tag{C5}$$

$$p_2^d = g_D^2 \frac{9}{64} \left(m_{20}^{\text{ini}}\right)^4 \frac{\omega_{\text{noise}}^2}{\Omega_L} \frac{\Gamma_0^2 \left(8\Gamma_2^2 + 8\Gamma_2\omega_{\text{noise}} + \omega_{\text{noise}}^2\right)}{(2\Gamma_2 + \omega_{\text{noise}})^3 \, G(\omega_{\text{noise}}, \mathbf{\Gamma})} [2\sin(2\theta) + 3\sin(4\theta)]^2, \tag{C6}$$

where $G(\omega_{\text{noise}}, \mathbf{\Gamma})$ is stated in Eq. (40) of the main text.

Irrelevance of the dispersive contributions

We note that we have not verified the predicted relations for the dispersive contributions of the line shape [see Eqs. (C5) and (C6). This is due to their contribution being below the noise floor of our system. We can verify that this is as expected for a Larmor frequency of approximately 9.45 kHz by calculating the ratios of the peak height equations and using the linewidths found in the experiment: $\Gamma_1 = 34$ Hz and $\Gamma_2 = 34$ Hz. We find p_1^d/p_1^a from Eq. (C5) divided by Eq. (39b) and we find p_2^d/p_2^a from Eq. (C6) divided by Eq. (39c). The calculations were done for the lowest white-noise amplitude of 7 mV$_{\text{rms}}$ and the highest white-noise amplitude of 3.5 V$_{\text{rms}}$. For V$_{\text{noise}} = 7$ mV$_{\text{rms}}$ we find $p_1^d/p_1^a = 1.1 \times 10^{-4}$ and $p_2^d/p_2^a = 3.2 \times 10^{-4}$. Furthermore, when V$_{\text{noise}} = 3.5$ V$_{\text{rms}}$ we find $p_1^d/p_1^a = 3.1 \times 10^{-5}$ and $p_2^d/p_2^a = 1.8 \times 10^{-4}$. Hence, the dispersive contribution is at least four orders of magnitude smaller than the absorptive contribution. Hence, this is significantly below our noise floor for both peaks, as seen experimentally.

APPENDIX D: AMPLITUDE CALIBRATION FOR THE NOISE SPECTRAL DENSITY $\omega_{\text{noise}} = 2\pi f_{\text{noise}}$

In order to determine the value of the constant c relating the magnitude of the noise spectral density to the (RMS) amplitude of the voltage applied in the noise generator, i.e., $\omega_{\text{noise}} = 2\pi f_{\text{noise}} = 2\pi c V^2_{\text{noise}}$, we directly measure the current in the coil that induces the noisy magnetic field. The signal from the generator, however, is first transformed thorough a 1-MHz low-pass filter to prevent the effect of aliasing, as well as a 1-kHz high-pass filter to eliminate any spurious contributions at very low (DC-like) frequencies. We record 100 traces of 0.01-s duration of the current reaching the coil (sampled at 40 MHz), while varying the voltage amplitude in the noise generator. Based on these we compute the PSD (30), which is presented in Fig. 7(a) in the units of Hz^2/Hz, after performing adequate rescaling given the values of the coil calibration factor (10.1 nT/mV$_{\text{rms}}$) and the gyromagnetic ratio of caesium (3.5 Hz/nT).

From Fig. 7(a) we can determine f_{noise} by seeing how the PSD varies with different white-noise amplitudes. We average areas of Fig. 7(a) in five different frequency ranges [specified in the label of Fig. 7(b)] to obtain the effective value of f_{noise} as a function of the noise amplitude: five values of V_{noise}

(stated in mV_{rms}) are used. For each of the averaged ranges, we then fit the quadratic dependence $f_{noise} = cV_{noise}^2$, which allows us to overall obtain $c = 1.33(3) \times 10^{-5}$ Hz/mV_{rms}^2 [see Fig. 7(b)].

[1] D. Budker and M. Romalis, Optical magnetometry, Nat. Phys. **3**, 227 (2007).

[2] *Optical Magnetometry*, edited by D. Budker and D. F. Jackson Kimball (Cambridge University Press, Cambridge, 2013).

[3] I. K. Kominis, T. W. Kornack, J. C. Allred, and M. V. Romalis, A subfemtotesla multichannel atomic magnetometer, Nature (London) **422**, 596 (2003).

[4] Gem Systems, https://www.gemsys.ca.

[5] QuSpin, https://quspin.com.

[6] Twinleaf, https://twinleaf.com.

[7] Fieldline Inc., https://fieldlineinc.com.

[8] MAG4Health, https://www.mag4health.com.

[9] G. Bison, N. Castagna, A. Hofer, P. Knowles, J.-L. Schenker, M. Kasprzak, H. Saudan, and A. Weis, A room temperature 19-channel magnetic field mapping device for cardiac signals, Appl. Phys. Lett. **95**, 173701 (2009).

[10] R. Wyllie, M. Kauer, R. T. Wakai, and T. G. Walker, Optical magnetometer array for fetal magnetocardiography, Opt. Lett. **37**, 2247 (2012).

[11] K. Jensen, M. A. Skarsfeldt, H. Stærkind, J. Arnbak, M. V. Balabas, S.-P. Olesen, B. H. Bentzen, and E. S. Polzik, Magnetocardiography on an isolated animal heart with a room-temperature optically pumped magnetometer, Sci. Rep. **8**, 16218 (2018).

[12] H. Xia, A. Ben-Amar Baranga, D. Hoffman, and M. V. Romalis, Magnetoencephalography with an atomic magnetometer, Appl. Phys. Lett. **89**, 211104 (2006).

[13] E. Boto *et al.*, Moving magnetoencephalography towards real-world applications with a wearable system, Nature (London) **555**, 657 (2018).

[14] *Flexible High Performance Magnetic Field Sensors: On-Scalp Magnetoencephalography and Other Applications*, edited by E. Labyt, T. Sander, and R. Wakai (Springer, Berlin, 2022).

[15] L. Marmugi and F. Renzoni, Optical magnetic induction tomography of the heart, Sci. Rep. **6**, 23962 (2016).

[16] K. Jensen, M. Zugenmaier, J. Arnbak, H. Stærkind, M. V. Balabas, and E. S. Polzik, Detection of low-conductivity objects using eddy current measurements with an optical magnetometer, Phys. Rev. Res. **1**, 033087 (2019).

[17] A. Wickenbrock, N. Leefer, J. W. Blanchard, and D. Budker, Eddy current imaging with an atomic radio-frequency magnetometer, Appl. Phys. Lett. **108**, 183507 (2016).

[18] P. Bevington, R. Gartman, and W. Chalupczak, Enhanced material defect imaging with a radio-frequency atomic magnetometer, J. Appl. Phys. **125**, 094503 (2019).

[19] C. Deans, L. Marmugi, and F. Renzoni, Active underwater detection with an array of atomic magnetometers, Appl. Optics **57**, 2346 (2018).

[20] L. M. Rushton, T. Pyragius, A. Meraki, L. Elson, and K. Jensen, Unshielded portable optically pumped magnetometer for the remote detection of conductive objects using eddy current measurements, Rev. Sci. Instrum. **93**, 125103 (2022).

[21] W. Wasilewski, K. Jensen, H. Krauter, J. J. Renema, M. V. Balabas, and E. S. Polzik, Quantum noise limited and entanglement-assisted magnetometry, Phys. Rev. Lett. **104**, 133601 (2010).

[22] W. Chalupczak, R. M. Godun, S. Pustelny, and W. Gawlik, Room temperature femtotesla radio-frequency atomic magnetometer, Appl. Phys. Lett. **100**, 242401 (2012).

[23] D. A. Keder, D. W. Prescott, A. W. Conovaloff, and K. L. Sauer, An unshielded radio-frequency atomic magnetometer with sub-femtotesla sensitivity, AIP Adv. **4**, 127159 (2014).

[24] M. P. Ledbetter, V. M. Acosta, S. M. Rochester, D. Budker, S. Pustelny, and V. V. Yashchuk, Detection of radio-frequency magnetic fields using nonlinear magneto-optical rotation, Phys. Rev. A **75**, 023405 (2007).

[25] L. M. Rushton, L. Elson, A. Meraki, and K. Jensen, Alignment-based optically pumped magnetometer using a buffer-gas cell, Phys. Rev. Appl. **19**, 064047 (2023).

[26] W. Happer, Optical pumping, Rev. Mod. Phys. **44**, 169 (1972).

[27] A. Weis, G. Bison, and A. S. Pazgalev, Theory of double resonance magnetometers based on atomic alignment, Phys. Rev. A **74**, 033401 (2006).

[28] T. Zigdon, A. D. Wilson-Gordon, S. Guttikonda, E. J. Bahr, O. Neitzke, S. M. Rochester, and D. Budker, Nonlinear magneto-optical rotation in the presence of a radio-frequency field, Opt. Express **18**, 25494 (2010).

[29] F. Beato, E. Belorizky, E. Labyt, M. Le Prado, and A. Palacios-Laloy, Theory of a ^{4}He parametric-resonance magnetometer based on atomic alignment, Phys. Rev. A **98**, 053431 (2018).

[30] F. Bertrand, T. Jager, A. Boness, W. Fourcault, G. Le Gal, A. Palacios-Laloy, J. Paulet, and J. M. Léger, A ^{4}He vector zero-field optically pumped magnetometer operated in the earth-field, Rev. Sci. Instrum. **92**, 105005 (2021).

[31] G. Colangelo, R. J. Sewell, N. Behbood, F. M. Ciurana, G. Triginer, and M. W. Mitchell, Quantum atom-light interfaces in the gaussian description for spin-1 systems, New J. Phys. **15**, 103007 (2013).

[32] M. Auzinsh, D. Budker, and S. M. Rochester, *Optically Polarized Atoms: Understanding Light-Atom Interactions* (Oxford University Press, Oxford, 2014).

[33] N. A. Sinitsyn and Y. V. Pershin, The theory of spin noise spectroscopy: a review, Rep. Prog. Phys. **79**, 106501 (2016).

[34] C. Gardiner and P. Zoller, *Quantum Noise* (Springer, Berlin, 2000).

[35] V. S. Zapasskii, A. Greilich, S. A. Crooker, Y. Li, G. G. Kozlov, D. R. Yakovlev, D. Reuter, A. D. Wieck, and M. Bayer, Optical spectroscopy of spin noise, Phys. Rev. Lett. **110**, 176601 (2013).

[36] P. Glasenapp, N. A. Sinitsyn, L. Yang, D. G. Rickel, D. Roy, A. Greilich, M. Bayer, and S. A. Crooker, Spin noise spectroscopy beyond thermal equilibrium and linear response, Phys. Rev. Lett. **113**, 156601 (2014).

[37] V. Shah, G. Vasilakis, and M. V. Romalis, High bandwidth atomic magnetometery with continuous quantum nondemolition measurements, Phys. Rev. Lett. **104**, 013601 (2010).

[38] V. G. Lucivero, R. Jiménez-Martínez, J. Kong, and M. W. Mitchell, Squeezed-light spin noise spectroscopy, Phys. Rev. A **93**, 053802 (2016).

[39] Y. Wen, X. Li, G. Zhang, and K. Zhao, Zero-field spin-noise spectrum of an alkali vapor with strong spin-exchange coupling, Phys. Rev. A **104**, 063708 (2021).
[40] K. Mouloudakis, G. Vasilakis, V. G. Lucivero, J. Kong, I. K. Kominis, and M. W. Mitchell, Effects of spin-exchange collisions on the fluctuation spectra of hot alkali-metal vapors, Phys. Rev. A **106**, 023112 (2022).
[41] K. Mouloudakis, F. Vouzinas, A. Margaritakis, A. Koutsimpela, G. Mouloudakis, V. Koutrouli, M. Skotiniotis, G. P. Tsironis, M. Loulakis, M. W. Mitchell, G. Vasilakis, and I. K. Kominis, Interspecies spin-noise correlations in hot atomic vapors, Phys. Rev. A **108**, 052822 (2023).
[42] A. A. Fomin, M. Y. Petrov, G. G. Kozlov, M. M. Glazov, I. I. Ryzhov, M. V. Balabas, and V. S. Zapasskii, Spin-alignment noise in atomic vapor, Phys. Rev. Res. **2**, 012008(R) (2020).
[43] A. A. Fomin, M. Y. Petrov, I. I. Ryzhov, G. G. Kozlov, V. S. Zapasskii, and M. M. Glazov, Nonlinear spectroscopy of high-spin fluctuations, Phys. Rev. A **103**, 023104 (2021).
[44] S. Liu, P. Neveu, J. Delpy, L. Hemmen, E. Brion, E. Wu, F. Bretenaker, and F. Goldfarb, Birefringence and dichroism effects in the spin noise spectra of a spin-1 system, New J. Phys. **24**, 113047 (2022).
[45] S. Liu, P. Neveu, J. Delpy, E. Wu, F. Bretenaker, and F. Goldfarb, Spin-noise spectroscopy of a spin-one system, Phys. Rev. A **107**, 023527 (2023).
[46] J. Delpy, S. Liu, P. Neveu, E. Wu, F. Bretenaker, and F. Goldfarb, Spin-noise spectroscopy of optical light shifts, Phys. Rev. A **107**, L011701 (2023).
[47] J. Delpy, S. Liu, P. Neveu, C. Roussy, T. Jolicoeur, F. Bretenaker, and F. Goldfarb, Creation and dynamics of spin fluctuations in a noisy magnetic field, New J. Phys. **25**, 093055 (2023).
[48] R. Jiménez-Martínez, J. Kołodyński, C. Troullinou, V. G. Lucivero, J. Kong, and M. W. Mitchell, Signal tracking beyond the time resolution of an atomic sensor by kalman filtering, Phys. Rev. Lett. **120**, 040503 (2018).
[49] J. Kitching, Chip-scale atomic devices, Appl. Phys. Rev. **5**, 031302 (2018).
[50] S. M. Rochester and D. Budker, Atomic polarization visualized, Am. J. Phys. **69**, 450 (2001).
[51] I. H. Deutsch and P. S. Jessen, Quantum control and measurement of atomic spins in polarization spectroscopy, Opt. Commun. **283**, 681 (2010).
[52] C. Troullinou, R. Jiménez-Martínez, J. Kong, V. G. Lucivero, and M. W. Mitchell, Squeezed-light enhancement and backaction evasion in a high sensitivity optically pumped magnetometer, Phys. Rev. Lett. **127**, 193601 (2021).
[53] I. M. Savukov and M. V. Romalis, Effects of spin-exchange collisions in a high-density alkali-metal vapor in low magnetic fields, Phys. Rev. A **71**, 023405 (2005).
[54] I. M. Savukov, Spin exchange relaxation free (serf) magnetometers, in *High Sensitivity Magnetometers*, edited by A. Grosz, M. J. Haji-Sheikh, and S. C. Mukhopadhyay (Springer, Cham, 2017), pp. 451–491.
[55] K. Mouloudakis and I. K. Kominis, Spin-exchange collisions in hot vapors creating and sustaining bipartite entanglement, Phys. Rev. A **103**, L010401 (2021).
[56] O. Katz, R. Shaham, and O. Firstenberg, Quantum interface for noble-gas spins based on spin-exchange collisions, PRX Quantum **3**, 010305 (2022).
[57] G. Bevilacqua, E. Breschi, and A. Weis, Steady-state solutions for atomic multipole moments in an arbitrarily oriented static magnetic field, Phys. Rev. A **89**, 033406 (2014).
[58] H.-P. Breuer and F. Petruccione, *The Theory of Open Quantum Systems* (Oxford University Press, Oxford, 2002).
[59] C. W. Gardiner, *Handbook of Stochastic Methods*, 3rd ed. (Springer, Berlin, 1985).
[60] A. Meraki, L. Elson, N. Ho, A. Akbar, M. Koźbiał, J. Kołodyński, and K. Jensen, Zero-field optical magnetometer based on spin alignment, Phys. Rev. A **108**, 062610 (2023).
[61] A. Akbar, M. Kozbiál, L. Elson, A. Meraki, J. Kolodyński, and K. Jensen, Optimized detection modality for double resonance alignment based optical magnetometer, arXiv:2403.05357.
[62] N. Wilson, C. Perrella, R. Anderson, A. Luiten, and P. Light, Wide-bandwidth atomic magnetometry via instantaneous-phase retrieval, Phys. Rev. Res. **2**, 013213 (2020).
[63] R. Li, F. N. Baynes, A. N. Luiten, and C. Perrella, Continuous high-sensitivity and high-bandwidth atomic magnetometer, Phys. Rev. Appl. **14**, 064067 (2020).
[64] S. Hao, H. Shi, C. N. Gagatsos, M. Mishra, B. Bash, I. Djordjevic, S. Guha, Q. Zhuang, and Z. Zhang, Demonstration of entanglement-enhanced covert sensing, Phys. Rev. Lett. **129**, 010501 (2022).
[65] V. G. Lucivero, A. Dimic, J. Kong, R. Jiménez-Martínez, and M. W. Mitchell, Sensitivity, quantum limits, and quantum enhancement of noise spectroscopies, Phys. Rev. A **95**, 041803(R) (2017).
[66] https://doi.org/10.17639/nott.7434.